remote sensing

MDPI

Article

Near-Time Measurement of Aerosol Optical Depth and Black Carbon Concentration at Socheongcho Ocean Research Station: Aerosol Episode Case Analysis

Soi Ahn [1,2], Meehye Lee [2,*], Hyeon-Su Kim [3], Eun-ha Sohn [3] and Jin-Yong Jeong [4]

[1] Environmental Satellite Center (ESC), National Institute of Environmental Research (NIER), Hwangyong-ro 42, Seogu, Incheon 22689, Republic of Korea; jjahn@korea.kr
[2] Atmosphere Environment Research, Korea University, Anam-ro 145, Seongbuk-gu, Seoul 02841, Republic of Korea
[3] National Meteorological Satellite Center (NMSC), Korea Meteorological Administration (KMA), Guam-gil 64-18, Jincheon-gun 27803, Republic of Korea; atmos1305@korea.kr (H.-S.K.); soneh431@korea.kr (E.-h.S.)
[4] Korea Institute of Ocean Science & Technology (KOIST), 385 Haeyang-ro, Yeongdo-gu, Busan Metropolitan City 49111, Republic of Korea; jyjeong@kiost.ac.kr (J.-Y.J.)
* Correspondence: meehye@korea.ac.kr; Tel.: +82-02-3290-5146

Abstract: This study examined the seasonal variations and influencing factors for black carbon (BC) concentrations and aerosol optical depth (AOD) at the Socheongcho Ocean Research Station (SORS) on the Korean Peninsula from July 2019 to December 2020. An AOD algorithm was developed and validated using the Geo-KOMPSAT-2A (GK-2A) satellite. The GK-2A AOD demonstrated comparable performance to that of Low Earth Orbit satellites, including the Terra/MODIS (R^2 = 0.86), Aqua/MODIS (R^2 = 0.83), and AERONET AODs (R^2 = 0.85). Multi-angle absorption photometry revealed that seasonal average BC concentrations were the highest in winter (0.91 ± 0.80 μg·m^{-3}), followed by fall (0.80 ± 0.66 μg·m^{-3}), wet summer (0.75 ± 0.55 μg·m^{-3}), and dry summer (0.52 ± 0.20 μg·m^{-3}). The seasonal average GK-2A AOD was higher in wet summer (0.45 ± 0.37 μg·m^{-3}) than in winter. The effects of meteorological parameters, AERONET AOD wavelength, and gaseous substances on GK-2A AOD and BC were investigated. The SHapley Additive exPlanations-based feature importance analysis for GK-2A AOD identified temperature, relative humidity (RH), and evaporation as major contributors. BC concentrations were increased, along with $PM_{2.5}$ and CO levels, due to the effects of combustion processes during fall and winter. Analysis of high-aerosol-loading cases revealed an increase in the fine-mode fraction, emphasizing the meteorological effects on GK-2A AOD. Thus, long-range transport and local BC sources played a critical role at the SORS.

Keywords: aerosol optical depth; satellite; black carbon; Socheongcho; Geo-KOMPSAT-2A

Academic Editor: Xuewei Hou

Received: 16 December 2024
Revised: 17 January 2025
Accepted: 21 January 2025
Published: 23 January 2025

Citation: Ahn, S.; Lee, M.; Kim, H.-S.; Sohn, E.-h.; Jeong, J.-Y. Near-Time Measurement of Aerosol Optical Depth and Black Carbon Concentration at Socheongcho Ocean Research Station: Aerosol Episode Case Analysis. *Remote Sens.* **2025**, *17*, 382. https://doi.org/10.3390/rs17030382

1. Introduction

Aerosols significantly influence the Earth's radiation balance, as well as its hydrological and biogeochemical cycles [1]. Among these, carbonaceous aerosols, including black carbon (BC), are notable for their strong optical absorption properties, and are the key anthropogenic components of the atmospheric aerosol system. The levels of carbonaceous aerosols have risen significantly since preindustrial times, primarily due to emissions from the incomplete combustion of fossil fuels, various types of biomass and biofuels,

and exhaust from automobiles and aircraft, among other sources [2,3]. BC absorbs solar radiation, resulting in positive radiative forcing at the tropopause and negative forcing at the surface [4,5].

Recent research on the properties of BC and its influence on the atmosphere has been extensive, highlighting BC's significant role in climate change [6–9]. Understanding BC emissions from ocean research stations is particularly important for studying haze formation, regional carbonaceous particulate emissions, and transport, and assessing regional climate forcing [10]. The average atmospheric lifetime of BC in the lower troposphere is approximately one week, and is strongly influenced by meteorological conditions such as wind speed (WS), planetary boundary layer height (PBLH), and relative humidity (RH). Notably, BC's strong absorption properties reduce solar radiation, altering surface temperature and PBLH, which subsequently impacts cloud formation [11,12].

Aerosol optical depth (AOD), a key measure of aerosol optical properties, is an essential parameter for estimating direct aerosol radiative forcing. AOD is defined as the vertical column across the entire atmospheric column, from the Earth's surface to the top of the atmosphere (TOA), representing the attenuation of solar radiation due to aerosol scattering and absorption. Typically, AOD is obtained through ground-based or satellite-based observations. Ground-based observations offer high temporal and spectral resolutions with relatively simple retrieval methods; however, they only represent a localized area around the observation site. In contrast, satellite-based remote sensing provides systematic retrieval of optical aerosol properties over broader spatial scales.

Satellite-based AOD measurements have the advantages of wide spatial coverage and continuous observations, making them valuable for monitoring long-distance aerosol transport and concentration changes [13,14]. However, these retrieval algorithms are more complex and less accurate compared to ground-based methods, often leading to overestimation due to variations in surface reflectivity across spectral bands [15–18]. This issue is particularly pronounced in regions with high surface albedo during winter, such as basins, deserts, and snow-covered areas. Therefore, to maximize the utility of the satellite data's wide spatiotemporal coverage and minimize uncertainties in aerosol effect estimations, satellite observations must be validated against ground-based measurements.

We developed a visible AOD algorithm using the Geo-KOMPSAT-2A Advanced Meteorological Imager (GK-2A/AMI) for aerosol monitoring in East Asia, significantly improving its accuracy through the integration of GK-2A cloud data [19–23]. The GK-2A AOD algorithm reduced errors by employing high-accuracy cloud detection outputs across multiple channels (visible, infrared, and water vapor). However, uncertainty increased in regions with high surface reflectivity, such as deserts.

To validate the accuracy of satellite-derived aerosol data, previous studies have extensively utilized ground-based observations (e.g., AERONET) and other satellite datasets [19–23]. This study advances on such approaches by directly comparing satellite-derived data with ground-based BC observations, enabling a detailed assessment of aerosol characteristics, including scattering and absorption. Socheongcho, strategically located within a pathway of long-range atmospheric inflow and with a background atmosphere, provides an optimal site for investigating meteorological factors influencing high-concentration aerosol events.

These findings are expected to contribute substantially to policy initiatives aimed at mitigating air pollution, such as Korea's fine dust seasonal management system, particularly for addressing the seasonal transport of long-range pollutants. Furthermore, the results offer valuable recommendations for improving satellite AOD products to enhance their applicability in environmental monitoring and policy development.

2. Materials and Methods

2.1. Site Description and Surface Meteorological Conditions

The Socheongcho Ocean Research Station (SORS), located in the northern Yellow Sea (Figure 1), was established by the Korea Institute of Ocean Science and Technology (KIOST) in October 2014 [24]. It was constructed on a rock formation at a depth of 50 m, approximately 37 km south of Socheong Island (37°25′N, 124°44′E). The station currently houses 43 types of equipment, including 12 for weather observation, 22 for marine observation, and 7 for environmental monitoring. These instruments support oceanographic research, the identification of air pollutant transport routes, and investigations into typhoon structure and characteristics. Data from the SORS have been used to assess background fine dust concentrations on the Korean Peninsula and track changes in fine dust originating from external sources, underscoring the station's strategic importance in analyzing air pollution in Northeast Asia. KIOST has actively promoted international joint research on fine dust and established SORS as a key base for ground-based observations. In particular, air pollutant data from the station are critical for forecasting fine and ultrafine dust, which directly impact metropolitan areas. This study utilized SORS measurements of surface aerosol mass concentrations, aerosol optical properties, tropospheric gasses, and meteorological parameters collected between July 2019 and 31 December 2020.

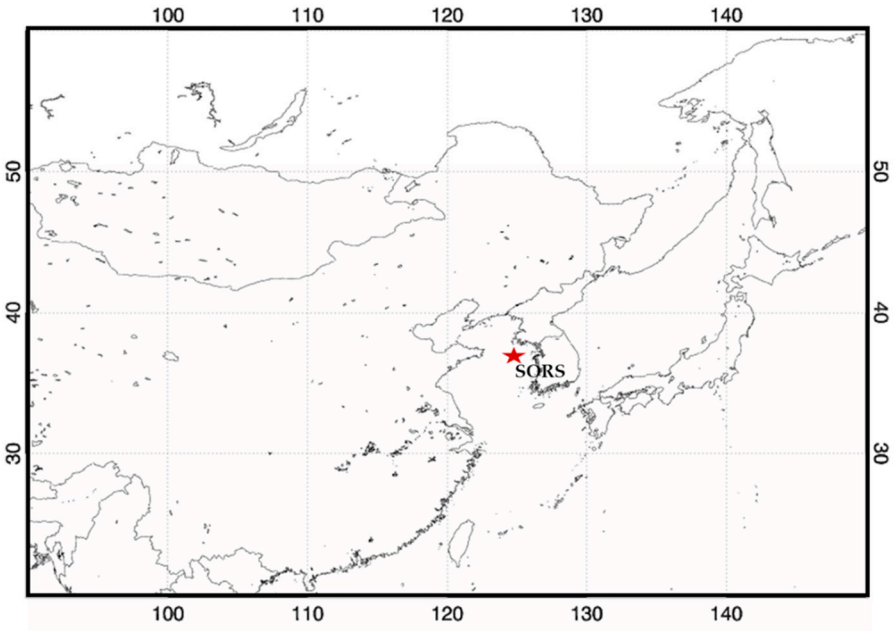

Figure 1. The location of the Socheongcho Ocean Research Station (SORS), marked with a red star, is shown in the Yellow Sea.

2.2. Instruments and Data

2.2.1. Ground-Based Studies

- BC and $PM_{2.5}$

Hourly measurements of $PM_{2.5}$ and BC during 2019–2020 were obtained using the beta (β)-ray absorption method (FH62C14, Thermo Fisher, 27 Forge Parkway Franklin, MA, USA) for $PM_{2.5}$ and a multi-angle absorption photometer (Model 5012 MAAP, Thermo Fisher, 27 Forge Parkway Franklin, MA, USA) for BC. The multi-angle absorption photometer measured aerosol BC mass concentrations at a single nominal wavelength of 670 nm. The method determined aerosol optical absorption values by simultaneously measuring the radiation transmitted through a particle-loaded fiber filter and the scattered radiation [25]. The principle of multi-angle absorption photometry involves measuring signals scattered

at angles of 130° and 165° during a typical transmission measurement. Radiative processes were modeled using a radiative transfer scheme incorporating the particle-loaded filter, aerosol filter layer, and black filter. The model outputs included the single scattering albedo, ω_{filter}, and optical depth, τ_{filter}, of the aerosol-loaded filter layer, which aligned with the measured transmitted and reflected signals. Using these values, the multi-angle absorption photometer absorption coefficient (B_{MAAP}) was calculated using the following equation [26,27]:

$$B_{MAAP} = -\frac{A}{V}\left(1 - \omega_{filter}\right) \times \tau_{filter} \quad (1)$$

where B_{MAAP} is a method-dependent coefficient related to absorption, A is the filter spot area, and V is the sampled volume.

- AERONET AOD

AERONET (https://aeronet.gsfc.nasa.gov, last accessed 12 December 2023) is a global ground-based network of sun–sky photometers that provides AOD measurements at seven wavelengths (340, 380, 440, 551, 675, 870, and 1020 nm). It also supplies information on aerosol mass size distribution and implements rigorous quality control processes [28]. AERONET data have been widely used for satellite validation and aerosol characterization in numerous satellite instruments and algorithms [29,30]. The low uncertainty of AERONET AOD measurements, ranging from 0.01 to 0.02 in visible and near-infrared wavelengths (340–1640 nm), enhances their reliability [31–34].

This study utilized the AERONET Version 3 (V3) algorithm, which offers fully automated cloud screening and quality control to address measurement anomalies. Level 2.0 data, representing the highest quality, were employed for direct sunlight measurements [35,36]. The spectral dependence of AOD from AERONET was used to compute the Angstrom exponent (AE) in this study, α.

$$AOD_\lambda = \beta\lambda^{-\alpha} \quad (2)$$

where AOD_λ is the approximated AOD at the wavelength λ; β is Angstrom's turbidity coefficient, equal to AOD at λ = 1 μm; and α is the Angstrom exponent. The Angstrom exponent serves as a reliable indicator of the ratio of accumulation-mode (r < 1 μm) to coarse-mode (r > 1 μm) particles. Although α is commonly assumed to be independent of the wavelength, it is well-established that α exhibits dependence on λ [37,38]. In this study, α values were calculated for the wavelength intervals of 440–870 nm and 440–667 nm.

- Gasses

Carbon monoxide (CO), carbon dioxide (CO_2), and methane (CH_4) concentrations were measured using cavity ring-down spectroscopy (CRDS; Model G2401, Picarro Inc., 3105 Patrick Henry Dr. Santa Clara, CA, USA). Cavity ring-down spectroscopy is a direct, quantitative absorption technique that enhances light–matter interaction through an extended optical path within a high-finesse optical resonator, enabling ultrasensitive trace gas detection with high spatial and temporal resolution. Recent advancements in cavity ring-down spectroscopy technology have expanded its applications to fundamental molecular spectroscopy, atmospheric sensing, exhaled breath diagnostics, plasma diagnostics, kinetics studies, and aerosol extinction and absorption monitoring [39].

2.2.2. Satellite-Based Studies

- GK-2A/AMI

The Korea Meteorological Administration (KMA) utilized the geostationary meteorological satellite GK-2A to monitor meteorological phenomena, including yellow dust

and typhoons. To provide detailed hazardous weather forecasts, the satellite observed the Korean Peninsula every 2 min and the full disk every 10 min, operating continuously. GK-2A featured 16 channels with central wavelengths ranging from 0.47 to 13.1 μm. An algorithm was developed to account for the unique characteristics of each channel based on specific weather phenomena. Notably, three visible bands (blue, green, red) and one near-infrared band (0.86 μm) were employed to effectively monitor the optical properties of aerosols [40]. In this study, AMI-based AOD products were developed to enhance aerosol detection accuracy and surface reflectance measurements. The measurement accuracy was $\Delta\tau = \pm 0.10 \pm 0.3\tau$ over land, and $\Delta\tau = \pm 0.05 \pm 0.2\tau$ over the ocean.

- Terra and Aqua/Moderate Resolution Imaging Spectroradiometer (MODIS)

The MODIS is a low Earth orbit (LEO) sensor designed to characterize spatiotemporal global aerosol properties. It operates on the EOS Terra satellite, which follows a descending orbit over the equator at approximately 10:30 local solar time, and the Aqua satellite, which follows an ascending orbit at approximately 13:30 local solar time. The MODIS has consistently acquired daily global measurements across 36 spectral bands (410–1450 nm) at three spatial resolutions: 250 m, 500 m, and 1 km.

MODIS-based AOD products continue to be widely used in various studies, including this one, which utilized the Collection 6 Level 2 (L2) AOD products [41,42]. The MODIS L2 aerosol products (MOD04 for Terra and MYD04 for Aqua, collectively referred to as M*D04) were generated using two distinct algorithms: Deep Blue (DB: Deep_Blue_Aerosol_Optical_Depth_550_Land) and Dark Target (DT: Corrected_Optical_Depth_Land and Optical_Depth_Land_And_Ocean) [43,44]. The predicted uncertainties for the MODIS AOD products were reported as follows: for DT over land: $\Delta\tau = \pm 0.05 \pm 0.15\tau$; for DB over land: $\Delta\tau = \pm 0.20 \pm 0.05\tau$; and over the ocean: $\Delta\tau = \pm 0.03 \pm 0.05\tau$.

- Suomi-Polar-orbiting Partnership (S-NPP)/Visible Infrared Imaging Radiometer Suite (VIIRS)

The VIIRS is a cross-track scanning radiometer sensor onboard the S-NPP satellite [45]. Developed to replace the aging MODIS, the VIIRS is capable of observing a wide swath (~3000 km), which enhances its ability to monitor multiple areas simultaneously. In this study, the VIIRS aerosol Intermediate Product was utilized, and data were obtained from the NOAA National Centers for Environmental Information website (https://www.ncei.noaa.gov, accessed on 1 January 2019). The data were subjected to continuous assessment with uncertainty value ranges of [$\Delta\tau = -0.470\tau - 0.01$ (lower bound), $-0.0058\tau + 0.09$ (upper bound)] over land, and [$\Delta\tau = -0.238\tau + 0.01$ (lower bound), $0.194\tau + 0.048$ (upper bound)] over the ocean. The VIIRS aerosol data were utilized to validate the accuracy of the AOD in this study for high-aerosol-loading events.

2.3. Methods

2.3.1. GK-2A AOD Algorithm

The NMSC developed an algorithm to retrieve the AOD from the AMI clear-sky spectral reflectance (Figure 2). The output had a spatial resolution of 2 km and a temporal resolution of 10 min during the daytime. The AMI AOD algorithm performed calculations after removing bright surfaces, such as sun glint, deserts, and bare soil, to reduce uncertainty in surface reflection. In particular, it is novel that it included more accurate cloud detection and bright surface masking via its SWIR and IR channels. Also, it reduced seasonal temperature differences by using the average aerosol background field for 30 days before observation.

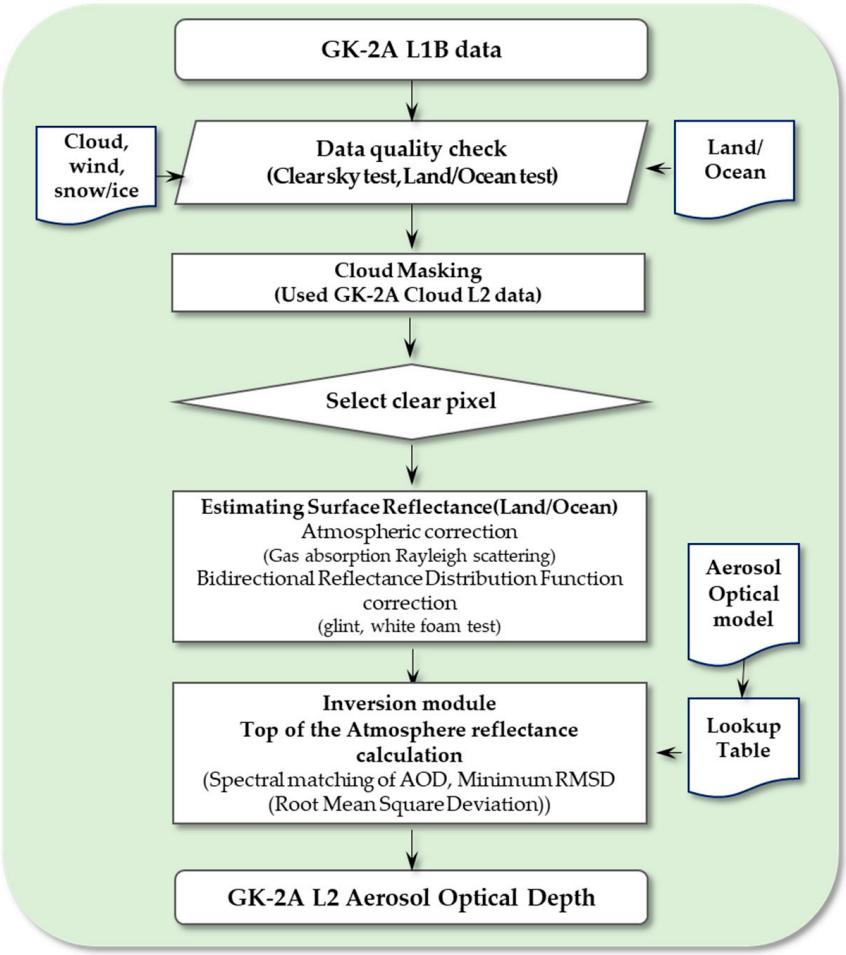

Figure 2. Flow chart of Geo-KOMPSAT-2A Advanced Meteorological Imager (GK-2A) aerosol optical depth (AOD) algorithm.

The multichannel aerosol algorithm's advantage was its ability to simultaneously retrieve optical depth and aerosol models by matching the observed TOA reflectance with pre-calculated values from selected AMI channels. This study used five-channel reflectance (0.47, 0.51, 0.64, 0.86, and 1.61 μm) from the GK-2A to select the appropriate aerosol optical property model and aerosol loading [19].

Step 1: Aerosol model assumption

The aerosol model, consisting of six categories [46], was derived from statistically determined aerosol size distributions in the AERONET databases for East Asia (49 stations, 1993–2018). Accurate aerosol optical properties were also determined through statistical analysis of the available data. The volume size distribution, an important AERONET inversion product, represents aerosol particle size distribution in a multimodal log-normal form, as follows:

$$\frac{dV(r)}{dlnr} = \sum_{i=1}^{n} \frac{C_{v,\,i}}{\sigma_i \sqrt{2\pi}} exp\left[-\frac{(\ln r - \ln r_{v,i})^2}{2\sigma_i^2}\right] \quad (3)$$

where i is the index of the log-normal aerosol mode, and n is the number of modes. For each mode, $C_{v,\,i}$ isrepresents the volume concentration of the aerosol particles, $r_{v,i}$ is the geometric mean radius, σ_i is the geometric standard deviation, and r is the particle radius [47,48].

Although sensitivity varies qualitatively by aerosol type, radiation sensitivity to AOD is higher in the short-wavelength region and decreases toward the long-wavelength region. This finding was determined using lookup tables (LUTs) that classified fine particle aerosols

in East Asia through a radiative transfer model. The radiation sensitivity decreased significantly in the shortwave-infrared region; however, it remained high in the visible region (channels 1 to 4). The aerosol model was developed through optimization based on the optical and physical properties of different aerosol types, leading to the sub-categorization of the aerosol-type model.

Step 2: AOD LUT

Six aerosol models were constructed using AERONET data, and LUTs were generated using a radiative transfer model. Table 1 lists the input variables for the Santa Barbara Discrete Ordinate Radiative Transfer model, part of the libRadtran software package (version 2.0.1, http://libradtran.org, accessed 2 February 2022) [49,50]. The LUTs were constructed as functions of scattering and absorbing AOD, optical properties, wavelengths, and extinction coefficients [51].

Table 1. The input variables used for the calculation of the aerosol optical depth (AOD) lookup tables.

Variable	Number of Entries	Entries
Wavelength	7	0.47, 0. 51, 0.64, 0.86, 1.37, 1.61, 3.83 μm (considering spectral response function)
Solar zenith angle	9	0, 10, 20, 30, . . ., 80° (10 intervals)
Satellite zenith angle	17	0, 5, 10, 15, . . ., 80° (5 intervals)
Relative azimuth angle	18	0, 10, 20, 30, . . ., 170° (10 intervals)
AOD	10	0.0, 0.3, 0.6, 0.9, 1.2, 1.5, 2.0, 3.0, 4.0, 5.0
AOD model	6	ASIA_AEROSOL_AMI_CAT1 ASIA_AEROSOL_AMI_CAT2 ASIA_AEROSOL_AMI_CAT3 ASIA_AEROSOL_AMI_CAT4 ASIA_AEROSOL_AMI_CAT5 ASIA_AEROSOL_AMI_CAT6

Step 3: Surface reflectance estimation

- Ocean

Radiance from the ocean surface depends on whitecaps, sun glint, and subsurface scattering, which are primarily influenced by WS and absorbing properties. The combination of these factors (ρ_{BRDF}) leads to the following parameterization [52]:

$$\rho_{BRDF} = \rho_{Foam}\ (\lambda) + (1 - \mathrm{A}_{Foam})\rho_{sunglint} + (1 - \rho_{Foam})\rho_{subwater} \quad (4)$$

The first term, ρ_Foam, represents the reflectance of foam patches and streaks caused by whitecaps, determined by the fraction covered by $A_{Foam} = 2.951 \times 10^{-6} \times Windspeed^{3.52}$ [53]. The second term, $(1 - \mathrm{A}_{Foam})\rho_{sunglint}$, represents the specular reflectance from the water surface without foam. This component can be calculated using the Fresnel formula for a flat surface, and depends on the angles of incidence and reflection, as well as the refractive index of water. In the spectral range, the refractive index decreases, which broadens and reduces the sun glint in rough ocean conditions [54]. The weighted factor $(1 - A_{Foam})$ represents the area not encompassed by whitecaps, as specular reflection occurs only in these regions. Additionally, $(1 - \rho_{Foam})\rho_{subwater}$ describes the reflectance due to subsurface light. The value of $\rho_{subwater}$ is influenced by scattering from water molecules and suspended particles in the water, in the absence of whitecaps [55].

- Land

The surface reflectance for overland aerosol retrievals was inferred using a hybrid method, based on background images pre-constructed from 30-day minimum reflectance

composites obtained from the GK-2A COMPADP. These composites provided clear sky conditions with the lowest aerosol loading. Composite images, corrected for atmospheric transmission, served as a surface reflectance database, even for bright surfaces such as deserts or urban areas.

Step 4: TOA reflectance calculation for LUTs

The aerosol retrieval algorithm used the L1B calibrated reflectance at the TOA from the visible and near-infrared channels of the AMI as primary inputs. The TOA approach determines the reflectance at a given AMI band. According to Equation (4), the spectral reflectance at the satellite level, ρ_{TOA}, is the combination of three components. The atmospheric contribution includes reflection, scattering, and absorption by aerosols and gasses.

$$\rho_{TOA} = \rho_{Rayleigh} + \rho_{Aerosol} + \frac{T_{trans}(\lambda)\cdot\rho_{sfc}(\lambda)}{1 - s(\lambda)\cdot\rho_{sfc}(\lambda)} \quad (5)$$

where ρ_{TOA} is the apparent reflectance, ρ_{sfc} is the surface reflectance, $\rho_{Rayleigh}$ is the Rayleigh reflectance, T_{trans} is the bi-directional transmittance, and $s(\lambda)$ is the spherical albedo.

Step 5: Retrieval of AOD

The aerosol reflectance was used to derive the AOD by applying the LUT to the optimal aerosol model. The SSM technique was employed to select the best LUT. This technique compares the aerosol reflectance from satellite observations with various LUTs for a given sun–satellite geometry. The first step involved determining the theoretical AOD (τ^*_{550}) from the satellite-estimated aerosol reflectance at 0.47 (ρ^{Sat}_{Aer}) using the function AOD ($\tau^*_{550} = f(\rho^{Sat}_{Aer})$). To achieve an accurate match with the observation, a set of ρ values within the LUT must align closely with the observed values in each channel. The differences between the calculated and observed ρ values were quantified using the root-mean-square deviation (RMSD).

$$RMSD = \frac{1}{N}\sqrt{\frac{\rho^{Calc}_{Aer}(\lambda_i) - \rho^{obs}_{Aer}(\lambda_i)}{\rho^{Calc}_{Aer}(\lambda_i)}} \quad (6)$$

where N is the number of selected wavelengths, ρ^{Calc}_{Aer} is the ρ calculated with the radiative transfer model, ρ^{obs}_{Aer} is the satellite-observed ρ, and λ_i is wavelength at 0.47, 0.51, 0.64, 0.86, and 1.61 μm.

The theoretical aerosol reflectance, ρ^*_{Aer}, at three channels (0.64, 0.86, 1.61 μm), and the RMSD between ρ^{Sat}_{Aer} and ρ^*_{Aer}, are simultaneously determined in this step. To determine τ^*_{550} and ρ^*_{Aer} for six aerosol models, the above process was repeated for each model. Finally, the AOD was determined based on the model that achieved the minimum RMSD [56–58].

2.3.2. Space and Time Coincidence

Spatiotemporal matching is essential for confirming the correlation between ground-based and satellite data. In this study, based on the SORS, the average satellite AOD value for a small pixel area was calculated and compared with the ground-based observation point. For spatial matching with the GK-2A AOD, the 10 km MODIS DB and DT AOD data were resampled to a 2 km resolution using the nearest-neighbor method [59]. To ensure temporal alignment, the average satellite observation data were matched to the ground observation period (1 h), with AERONET data available within a 1 h window centered on the MODIS overpass time.

2.3.3. Weighted Potential Source Contribution Function (WPSCF) Analysis

Air mass movement was quantified using a trajectory model, which effectively identified the transport pathways connecting source and receptor locations. However, the model involved deviations in air trajectories due to variations in spatial and vertical grids [60]. To minimize this deviation, the potential source contribution function (PSCF) was applied as a statistical analysis model. In this study, backward trajectories arriving at the SORS were traced from an altitude of 1000 m above ground level and ended at 12:00 UTC, with a duration of 72 h. These trajectories were calculated every 23 h (00:00–23:00 UTC) using NOAA's version 4 Hybrid Single-Particle Lagrangian Integrated Trajectory (HYSPLIT) model [61]. The PSCF method identified potential sources by combining backward trajectories with defined air pollutant values [62]. The study area was divided into small, equal grid cells, and the PSCF was calculated as follows:

$$PSCF_{ij} = \frac{m_{ij}}{n_{ij}} \tag{7}$$

Here, i and j represent the latitude and longitude, n_{ij} denotes the total number of endpoints passing through the ij cell, and m_{ij} represents the number of endpoints in the same cell associated with samples exceeding the criterion value (75th percentile).

To reduce uncertainty in the cells, the WPSCF was applied. A weight function, W(n_{ij}), was multiplied by the PSCF values when n_{ij} was less than three times the average number of trajectory endpoints (n_{mean}) in each cell. The WPSCF and weight function, W_{ij}, are defined as follows:

$$WPSCF_{ij} = \frac{m_{ij}}{n_{ij}} \times W(n_{ij}) \tag{8}$$

$$W_{ij} = \begin{cases} 1.00 & n_{ij} > 80 \\ 0.70 & 20 < n_{ij} \leq 80 \\ 0.42 & 10 < n_{ij} \leq 20 \\ 0.17 & n_{ij} \leq 20 \end{cases} \tag{9}$$

where *Average* is the average number of endpoints in each cell.

3. Results and Discussion

3.1. Performance of the GK-2A/AMI AOD Algorithm

3.1.1. Validation of GK-2A AOD

To quantitatively validate the GK-2A/AMI AODs, Terra and Aqua MODIS AODs were compared with ground-based observations (AERO_AOD) (Figure 3). One AERONET site, SORS, was selected for the analysis from July 2019 to December 2020. Standard deviations of the AERONET AODs, GK-2A AODs, and MODIS AODs (DT and DB) were calculated. The AODs from the GK-2A product developed in this study tended to slightly overestimate compared to LEO satellite AODs. However, the GK-2A AOD retrieval demonstrated strong agreement with ground-based AERONET data (R^2 = 0.85, slope = 1.01), outperforming the MODIS Aqua AODs, which showed lower accuracy (R^2 = 0.83, slope = 0.76). Moreover, the GK-2A AODs provided a higher temporal resolution (10 min) and spatial resolution (2 km) compared to the MODIS products. This allowed for the highest number of collocation-matching pixels (counts) to be obtained with AERONET. Consequently, the GK-2A AOD is highly effective for monitoring aerosol information in East Asia, due to its superior data acquisition capabilities compared to the other AOD products evaluated in this study.

The MODIS sensor, a polar-orbiting satellite (LEO), observes the Korean Peninsula twice daily. Consequently, the number of collocations is limited due to sampling constraints and cloud cover. Despite these limitations, the Terra MODIS exhibited a strong correlation

with ground observations (R^2 = 0.86, slope = 0.78), indicating high accuracy. However, the GK-2A AODs over the SORS were significantly overestimated, especially during episodes of high aerosol loading. Similar trends were observed with the Terra and Aqua MODIS AODs [63]. When precision was assessed using the RMSE with AERONET data as the true values, the following results were obtained: (a) GK-2A RMSE = 0.279, (b) Terra MODIS RMSE = 0.074, and (c) Aqua MODIS RMSE = 0.091. These findings demonstrated that the GK-2A AOD had a lower accuracy than the polar-orbiting MODIS products. Seasonal analysis (Figure 4) revealed an overestimation trend for the GK-2A AOD during wet summers, winters, and springs, coinciding with high aerosol concentrations. Despite this, the correlation between the AERONET and GK-2A AODs remained consistent across seasons: wet summer (R^2 = 0.84), winter (R^2 = 0.73), and spring (R^2 = 0.74). However, in dry summers and falls, the GK-2A AOD continued to overestimate low AOD values (0–1), and their relationship with the AERONET data was weaker, as evidenced by lower correlation coefficients in fall (R^2 = 0.76) and dry summer (R^2 = 0.67).

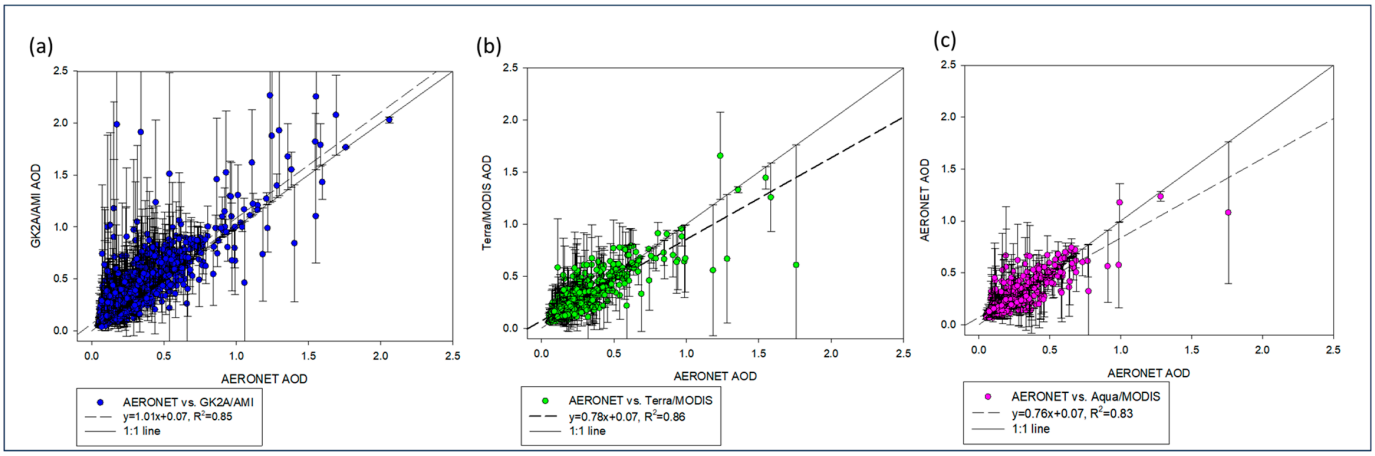

Figure 3. Aerosol optical depth (AOD) scatterplot of (**a**) GK-2A/AMI, (**b**) Terra/MODIS, and (**c**) Aqua/MODIS against ground-based reference AERONET data for 40 sites from July 2019 to December 2020. Dotted line shows linear regression, and black line is 1:1 line.

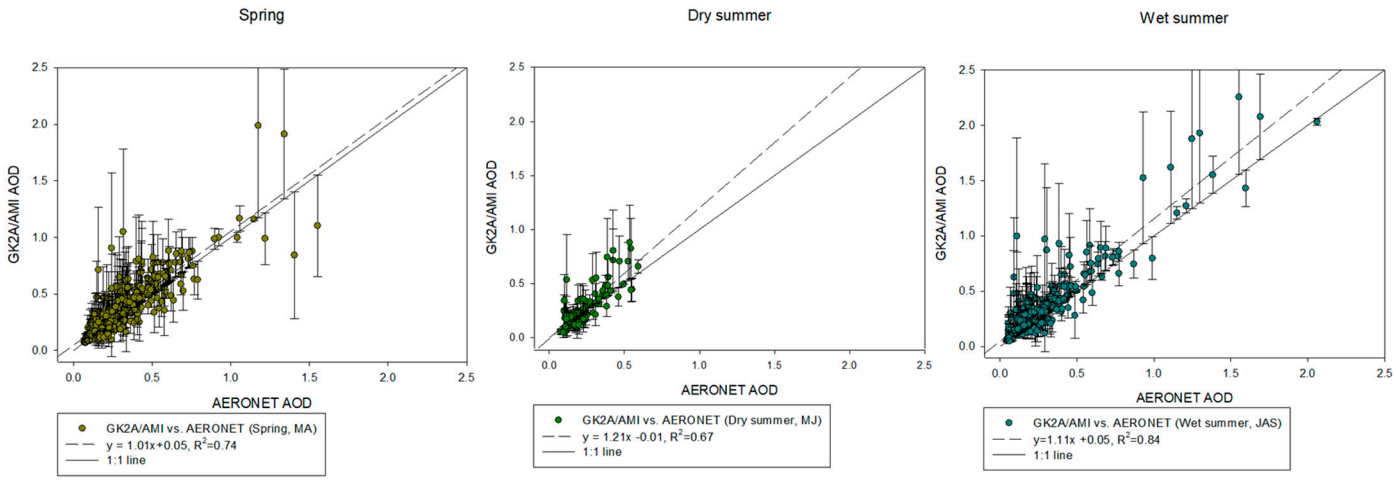

Figure 4. *Cont.*

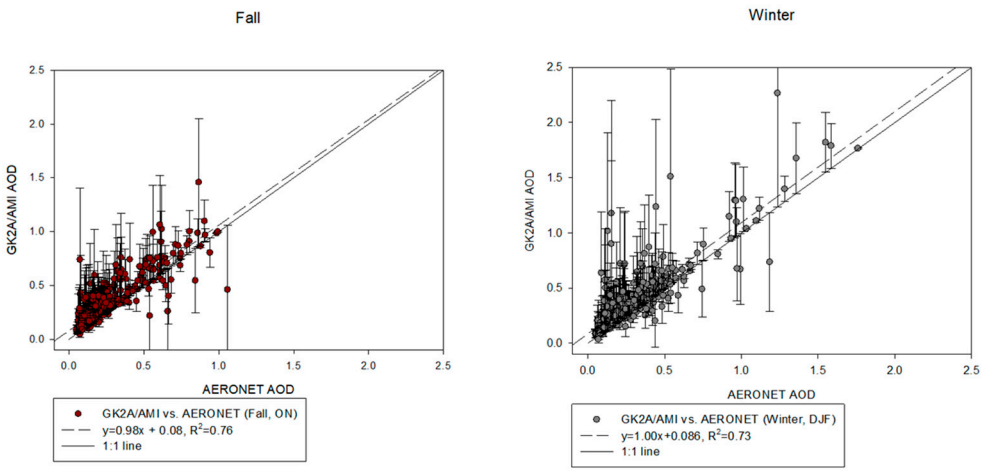

Figure 4. Seasonal scatterplots of GK-2A/AMI aerosol optical depth (AOD) against ground-based reference AERONET data for 40 sites from July 2019 to December 2020. Dotted line shows linear regression, and black line is 1:1 line.

3.1.2. Seasonal Distribution of AOD

The intra-annual variability of the GK-2A AOD and AE values at the SORS is presented as box-and-whisker plots in Figure 5a,b. The AOD values exhibited pronounced seasonality, peaking during the wet summer and reaching their lowest levels in the fall. The highest seasonal means of both the AOD and AE were observed in the wet summer season (0.448 ± 0.367 for AOD and 1.221 ± 0.353 for AE; monsoon, July–August–September), followed by fall (0.394 ± 0.199 for AOD and 1.181 ± 0.354 for AE, October–November), winter (0.407 ± 0.288 for AOD and 1.171 ± 0.365 for AE, December–January–February), spring (0.361 ± 0.246 for AOD and 1.209 ± 0.390 for AE, March–April), and dry summer (0.395 ± 0.228 for AOD and 1.282 ± 0.338 for AE, May–June). Monthly analysis (Figure 5c,d) revealed a rapid decrease in AOD values starting in September, reaching a minimum in November. Conversely, the AOD values increased sharply from April, peaking in July.

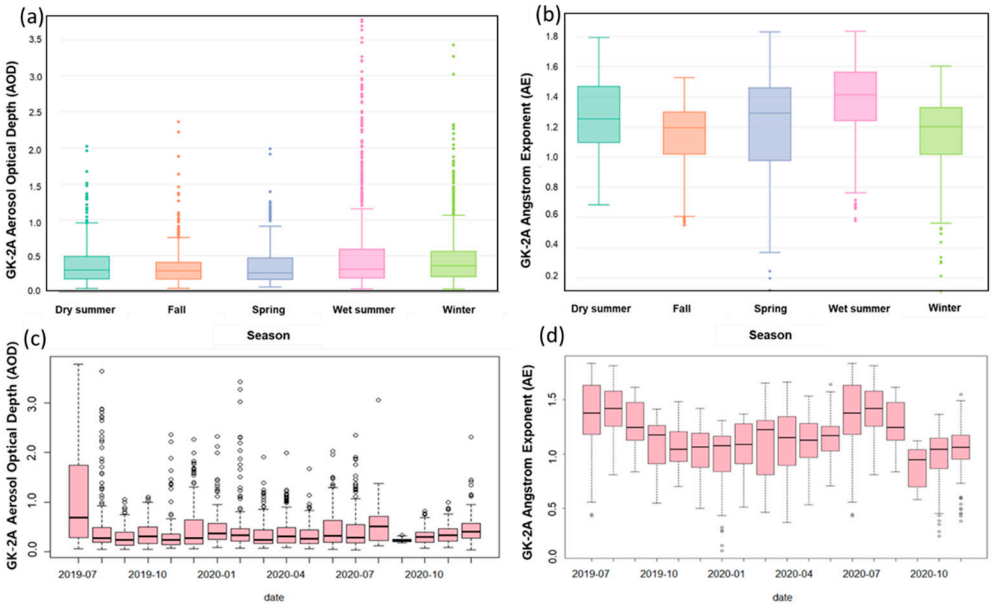

Figure 5. Seasonal (**a**,**b**) and monthly (**c**,**d**) variations in (a,**c**) GK-2A aerosol optical depth (AOD) and (**b**,**d**) GK-2A Angstrom Exponent (AE) at Socheongcho Ocean Research Station (SORS).

Atmospheric variability was the highest during the dry summer (June) and wet summer (July–August), particularly when the surface RH and temperature were elevated. These conditions accelerated the conversion of gasses to particulate matter and promoted the hygroscopic growth of water-soluble aerosols, resulting in elevated AOD levels [64]. In contrast, the AOD values were lower in August and September (0.6–0.7), primarily due to rain washout during the monsoon period. During winter, dry weather and low humidity further reduced the AOD values. However, high AOD levels were observed in cases of aerosol accumulation from fine dust generated in winter. These elevated AOD levels persisted for longer in industrial regions, such as densely populated areas of northern China, due to urbanization and land-use changes.

The low AE values (<1.0) during winter indicated the presence of mixed aerosols dominated by fine particles, which gradually increased to 1.0 due to enhanced anthropogenic activities. In spring (March–April), higher AOD values, coupled with lower AE values compared to other seasons, were partially attributed to yellow dust from long-distance transport. The SORS region provided a suitable location for assessing the impact of pollutants during spring, characterized by minimal dust storms and precipitation in northern China, serving as a background atmosphere [65]. Similar seasonal patterns were observed at the SORS, with one of the lowest AOD values recorded in fall (0.341 $\pm$ 0.195 in October and 0.338 $\pm$ 0.203 in November). This reduction in aerosol concentration was likely due to rapid atmospheric removal via precipitation [66].

3.2. Seasonal and Monthly Variations in BC Mass Concentration

3.2.1. Seasonal BC Characterization

During the analysis period, BC mass concentrations at the SORS, a background monitoring location, ranged from 1.5 $\mu g \cdot m^{-3}$ during summer to 4.0 $\mu g \cdot m^{-3}$ during winter. These variations were influenced by local emissions and meteorological factors, including boundary layer dynamics, wind patterns, RH, and long-range transport. Seasonal BC trends at the SORS were evident (Figure 6), with higher concentrations in winter and lower concentrations in summer. The seasonal mean BC concentrations were 0.908 $\pm$ 0.804 $\mu g \cdot m^{-3}$ (winter), 0.518 $\pm$ 0.199 $\mu g \cdot m^{-3}$ (pre-monsoon), 0.753 $\pm$ 0.549 $\mu g \cdot m^{-3}$ (monsoon), and 0.801 $\pm$ 0.655 $\mu g \cdot m^{-3}$ (post-monsoon). No data were available for spring (March–April 2020) due to instrument malfunction. The lowest monthly BC concentration occurred in August 2019, with an average value of 1.0 $\mu g \cdot m^{-3}$, which was approximately 50% of the October concentration (Figure 5b). BC concentrations across seasons were primarily influenced by emissions and meteorological conditions. High scavenging efficiency during summer likely reduced BC loadings. Additionally, anthropogenic BC emissions from fossil fuel usage in China were comparatively lower in summer and higher in winter, resulting in minimal BC concentrations during summer and significantly elevated levels in winter [67].

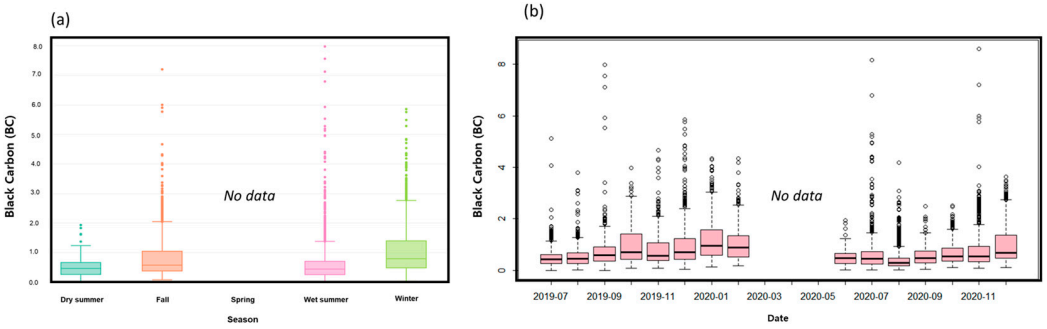

Figure 6. Seasonal (**a**) and monthly (**b**) variation in BC at the Socheongcho Ocean Research Station (SORS).

The shallow PBLH during winter, as determined by the Unified Model, increased pollutant concentrations near the Earth's surface by trapping them and limiting their dispersion compared to in the summer conditions. During winter at the SORS, northwesterly winds transported anthropogenic pollutants, primarily from northern China. The increased fossil fuel combustion during winter, driven by colder temperatures, led to a marked rise in open biomass burning for warmth. This combination of fossil fuel emissions, additional biomass burning, and a shallow PBLH resulted in elevated BC mass concentrations.

In contrast, BC mass concentrations decreased during the pre-monsoon period due to higher WSs and stronger shifts in the source region and wind direction. During this period, air masses originated from and traveled through less polluted regions in the west (marine areas). Back-trajectory analysis showed that over 80% of the air masses during this season originated from southern China, where BC emissions were relatively weaker compared to northern China [68].

The monsoon period also contributed to a decline in BC concentrations, with peak rainfall facilitating the efficient removal of aerosols through wet deposition. Additionally, strong thermal vertical convection and the full development of the PBLH in summer promoted the uplift of surface pollutants to higher altitudes, further reducing surface-level BC concentrations. As a result, BC levels decreased during summer 2019, but showed a significant increase throughout fall and winter. A similar seasonal pattern was observed in 2020. The seasonal variation in BC concentrations followed a regular pattern due to atmospheric dynamics, including PBLH, wind direction, WS, and long-range transport.

3.2.2. Analysis of GK-2A AODs and BC Concentrations

The SORS observations were influenced by urban pollution, dust, and biomass/biofuel burning from various sources. To understand the transport pathways of the GK-2A AOD and BC distributions, pollutant concentrations were analyzed based on wind direction and WS, focusing on the percentage of time concentrations that fell within specific ranges. This analysis utilized pollution rose plots to determine the dominant wind directions contributing to the overall concentrations (Figure 7). The GK-2A AOD and BC distributions displayed contrasting patterns. The GK-2A AODs exhibited higher concentrations in the southwest (SW), south (S), and southeast (SE) wind directions, with values exceeding 3–4. In contrast, BC concentrations were the highest in the northwest (NW) and west (W) wind directions, reaching 6.0–8.0 $\mu g\ m^{-3}$. Seasonal analyses confirmed a correlation between the elevated GK-2A AOD levels and SW, S, and SE winds during the wet summer (Figure 6b). Conditioning analyses were conducted to provide a more comprehensive understanding of these seasonal patterns. In winter, the GK-2A AOD concentrations increased in the NW wind direction, ranging between 1.5 and 2.0 $\mu g\ m^{-3}$, influencing both wet summer and winter patterns. However, the BC concentrations during fall and winter were significantly affected by NW, NNW, and north (N) winds, with notable increases observed in the west during winter and the north during fall.

To analyze the influence of source regions on the GK-2A AOD and BC distributions, 72 h backward airmass trajectories from the SORS were calculated for the analysis period. These trajectories validated atmospheric flow patterns at the observation point based on wind fields, and assessed the impact of long-distance transport. The WPSCF was employed to evaluate the seasonal distribution of pollutant sources at the SORS across various atmospheric layers. Seasonal WPSCF analyses were performed to investigate differences in air mass trajectories and potential aerosol source regions for the GK-2A AOD and BC levels. The mean GK-2A AOD concentrations during the analysis period were 0.5 ± 0.31. Seasonal variations in concentration were examined using trajectory analyses, with a focus on high AOD thresholds of 0.5 (Figure 8) and 1.0 (Figure 9). Similarly, the

mean BC concentration was 1.0 ± 0.31 μg m^{-3}. Seasonal changes were analyzed by setting BC thresholds of 1.0 μg m^{-3} (Figure 10) and 2.0 μg m^{-3} (Figure 11). The color scale in the figures represents the contributions from different aerosol emission sources.

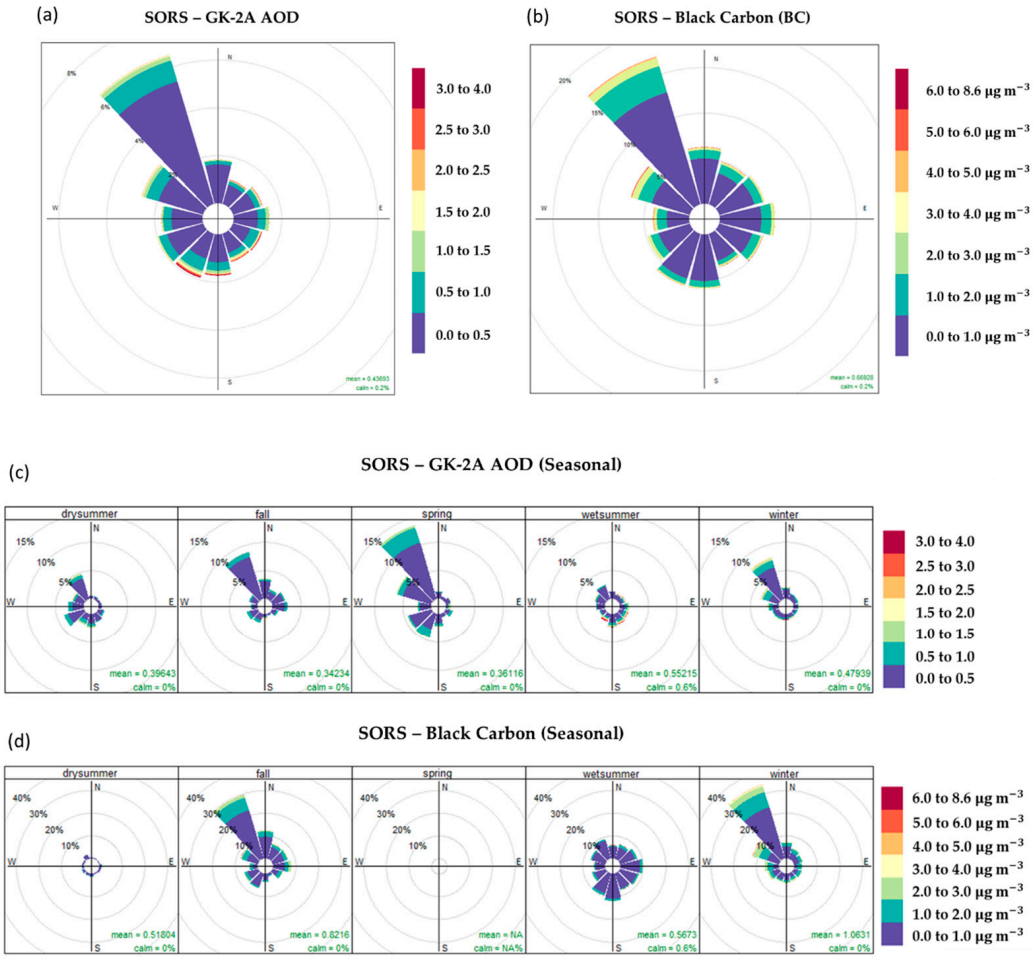

Figure 7. Pollutant distribution by wind direction and speed in Socheongcho Ocean Research Station (SORS): (**a**) GK-2A aerosol optical depth (AOD) and (**b**) BC. Seasonal distribution of (**c**) GK-2A AODs and (**d**) black carbon (BC).

The SORS was influenced by marine air masses from the Yellow Sea during the monsoon season (wet summer 2019), contributing to elevated AOD levels. Notably, high AOD values (>1.0, Figure 9a) were predominantly observed in the Yangtze River Delta (YRD) region and nearby cities, including Nanjing and Hangzhou, suggesting significant local contributions. The WPSCF values in the YRD exceeded 1.0, indicating that local emissions significantly influenced BC concentrations (Figure 11a). The YRD region, characterized by rapid industrial and urban development, has been a major source of BC emissions, impacting neighboring countries [69].

Seasonal analysis revealed that BC concentrations at the SORS exhibited strong seasonality, with high levels in autumn and low levels in summer. Both the GK-2A AODs and BC were transported over long distances from southern China during this period. However, during the post-monsoon season (fall 2019), aerosol sources diversified due to shifts in wind direction. Observations of BC concentrations at thresholds of 1.0 and 2.0 μg m^{-3} (Figures 10b and 11b) indicated that most inflows originated from Beijing in the northwest and Manchuria in the north, with Manchuria having a more significant impact during high-concentration events.

The GK-2A AODs, in contrast, were strongly influenced by emissions from NW and SW China. A particularly high AOD concentration in autumn, driven by extensive paddy crop residue burning, was comparable to the levels recorded during the wet summer of 2019 (Figures 8a and 9a) [70]. Additionally, industrial emissions from southern Jiangsu Province, including Shanghai, contributed to elevated BC levels, reaching 4.5 μg m^{-3}.

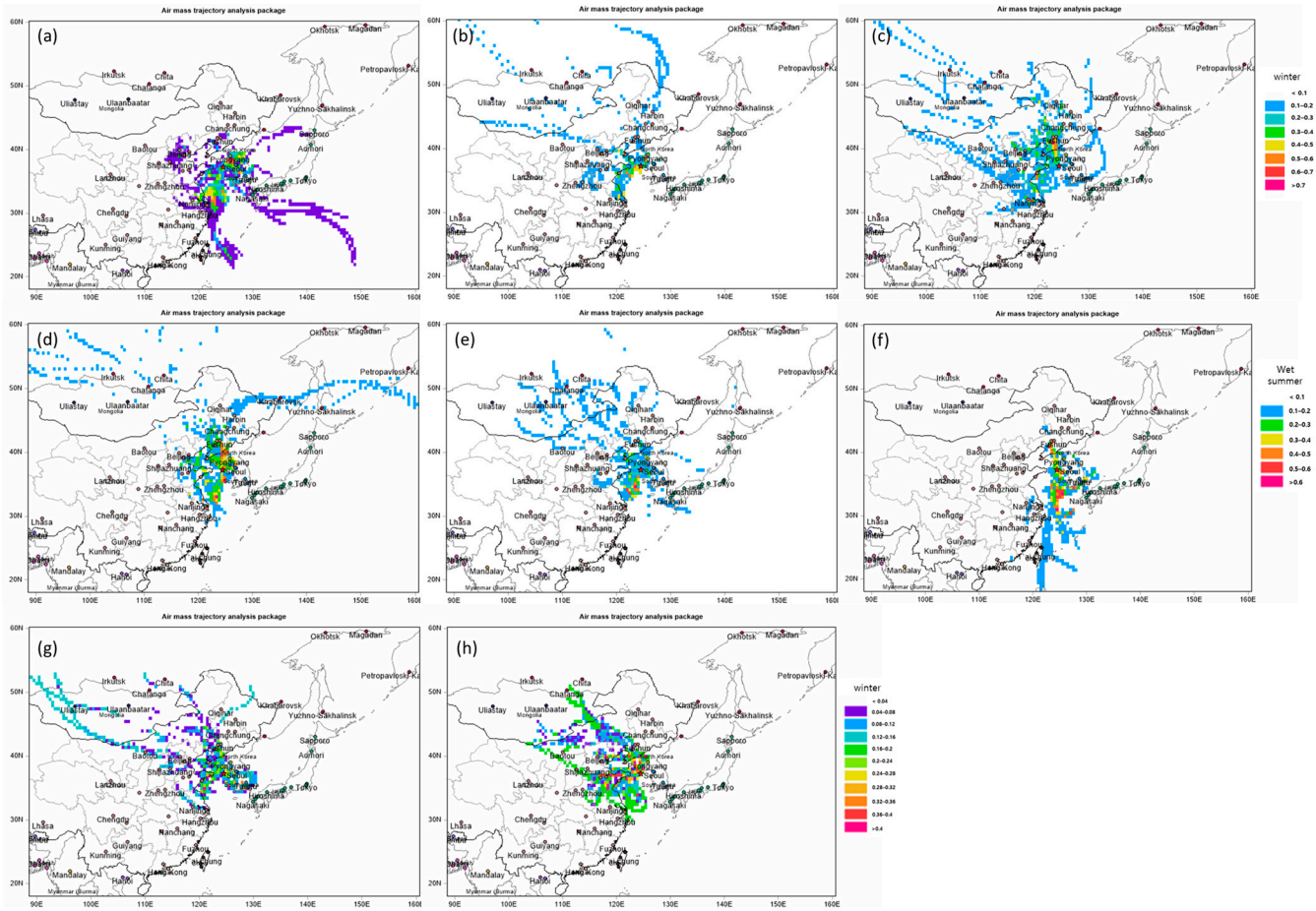

Figure 8. (**a**–**h**) Weighted potential source contribution function (WPSCF) results of 3-day back-trajectory of HYSPLIT Model for GK-2A aerosol optical depth (AOD) > 0.5 at Socheongcho Ocean Research Station (SORS) (standard).

The air pollutant trajectories during the winter of 2019 (Figures 10c and 11c) were classified into three clusters based on their source regions and transport paths. Cluster 1 represented dust sources originating in northwestern China, passing through central Inner Mongolia, and moving directly eastward toward the SORS. Cluster 2, which contributed more significantly to pollution at the SORS, followed an indirect route, originating from northern China, the south-central Beijing–Tianjin–Hebei region, and the central Shandong Peninsula, before heading southwest toward the SORS. Cluster 3 consisted of pollutants originating in northwestern China and traveling through eastern Inner Mongolia.

The WPSCF analysis (Figure 10) revealed that the Beijing–Tianjin–Hebei region was the most significant source of BC, with WPSCF values exceeding 1.0 μg m^{-3}. Contributions from northeastern China were relatively minor in comparison. For GK-2A AOD concentrations above 0.5 (Figure 8), the WPSCF model identified northwest China, including Anshan and Fushun, as key source regions. Northeast China, known as a heavily industrialized region, particularly in Anshan, experiences persistent pollution due to steel industry emissions [71].

The air masses from the northwest carried aerosols with similar characteristics to those observed during the post-monsoon period (fall 2019, Figures 8b, 9b, 10b and 11b). These air masses were transported over long distances from northwestern Asia; however, they were not heavily enriched with dust, due to the infrequency of yellow dust episodes during the analysis period.

In spring 2020, only AOD analysis was conducted, due to the unavailability of BC data. The WPSCF analysis for AOD concentrations exceeding 1.0 (Figure 9d) indicated that yellow dust influenced the SORS, primarily following the trajectory of cluster 1. During the dry summer of 2020, the pollutant trajectories (Figures 8e, 9e, 10e and 11e) were notably shorter than those in other seasons, highlighting a stronger regional influence compared to long-distance pollutant transport. The BC analysis (Figures 10e and 11e) revealed that high pollutant concentrations originating from Nagasaki, Japan, traveled through the Shandong Peninsula in China before reaching the SORS. This pattern suggests that many pollutants were locally generated within the Korean Peninsula, and that BC sources exhibited significant regional dependence during this period [72].

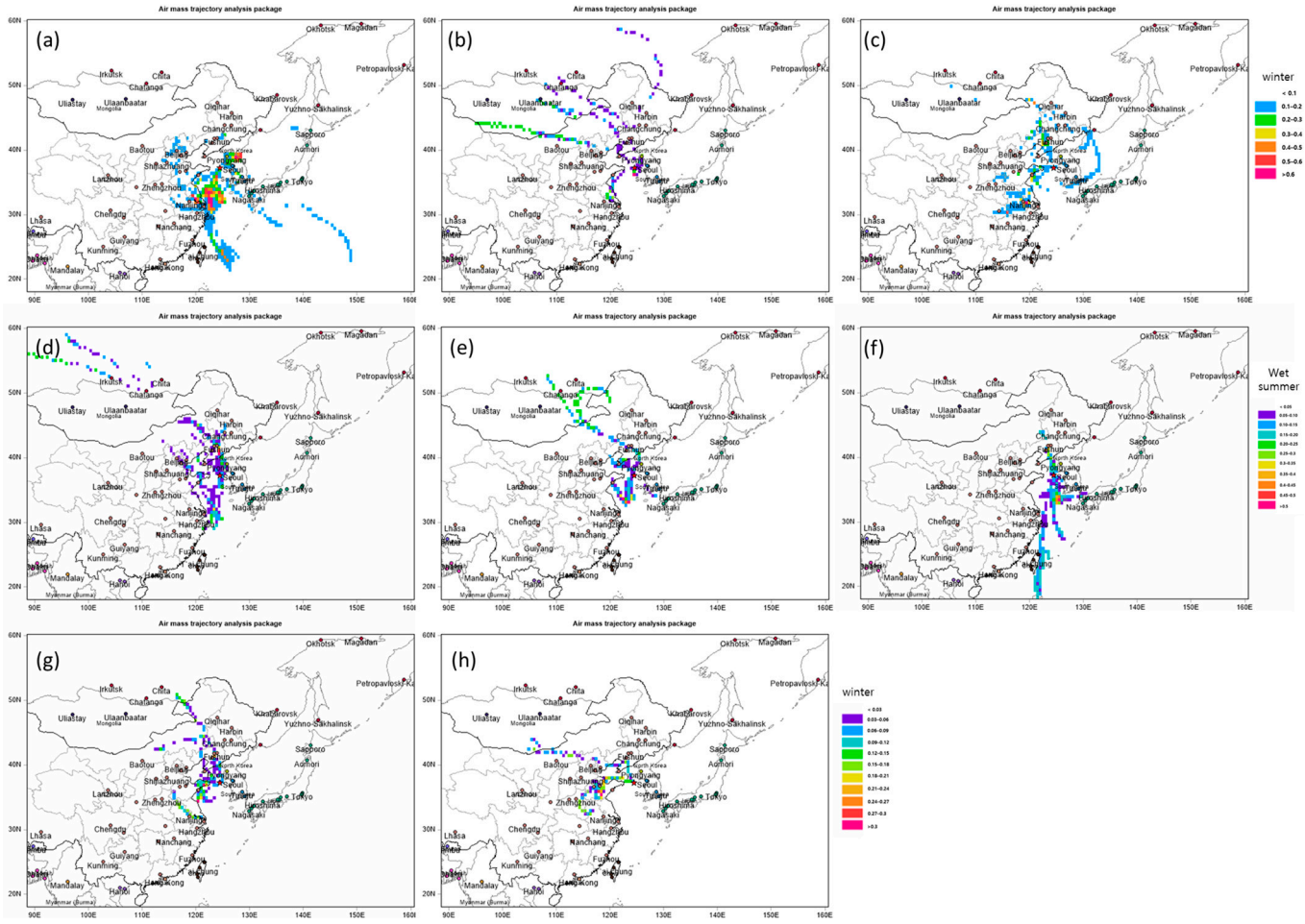

Figure 9. (**a**–**h**) Weighted potential source contribution function (WPSCF) result of 3-day back-trajectory of HYSPLIT Model for GK-2A aerosol optical depth (AOD) > 1.0 at Socheongcho Ocean Research Station (SORS) (standard).

The analysis of GK-2A AOD values ≥0.5 (Figure 8e) during the same period revealed an increase in AOD concentrations as pollutants generated in Japan traveled across the ocean, similar to the BC transport pattern. For AOD values ≥1.0 (Figure 9e), the SORS was affected by contaminants originating from Qingdao, located on the Shandong Peninsula, where coal energy sources are a significant contributor to air pollution [73]. A comparison

of the wet summers of 2019 and 2020 (Figures 8f, 9f, 10f and 11f) indicated that although the AOD and BC concentrations in 2020 were lower than in 2019, the pollutant transport pathways were similar. In 2020, AOD concentrations increased notably as pollutants passed over the Yellow Sea, exhibiting stronger scattering characteristics due to higher aerosol levels influenced by RH and hygroscopic growth factor, f(RH). Unusually, the SORS was also affected by pollutants from northwestern China, including Anshan and Fushun.

The BC transport pathways in 2020 were more diverse than in 2019, with rapidly moving pollutants originating from Taipei and Japan and slower-moving pollutants from steel mills in southern Korea. During the fall and winter of 2019 and 2020 (Figures 8g, 9g, 10g and 11g), pollutant pathways and concentrations were similar, although the AOD values were higher in the winter of 2020 (Figures 8h, 9h, 10h and 11h). Coarse particles dominated in spring due to yellow dust, while fine particles prevailed in summer due to hygroscopic growth. In fall and winter, a mixture of fine and coarse particles was observed, depending on the source region [74].

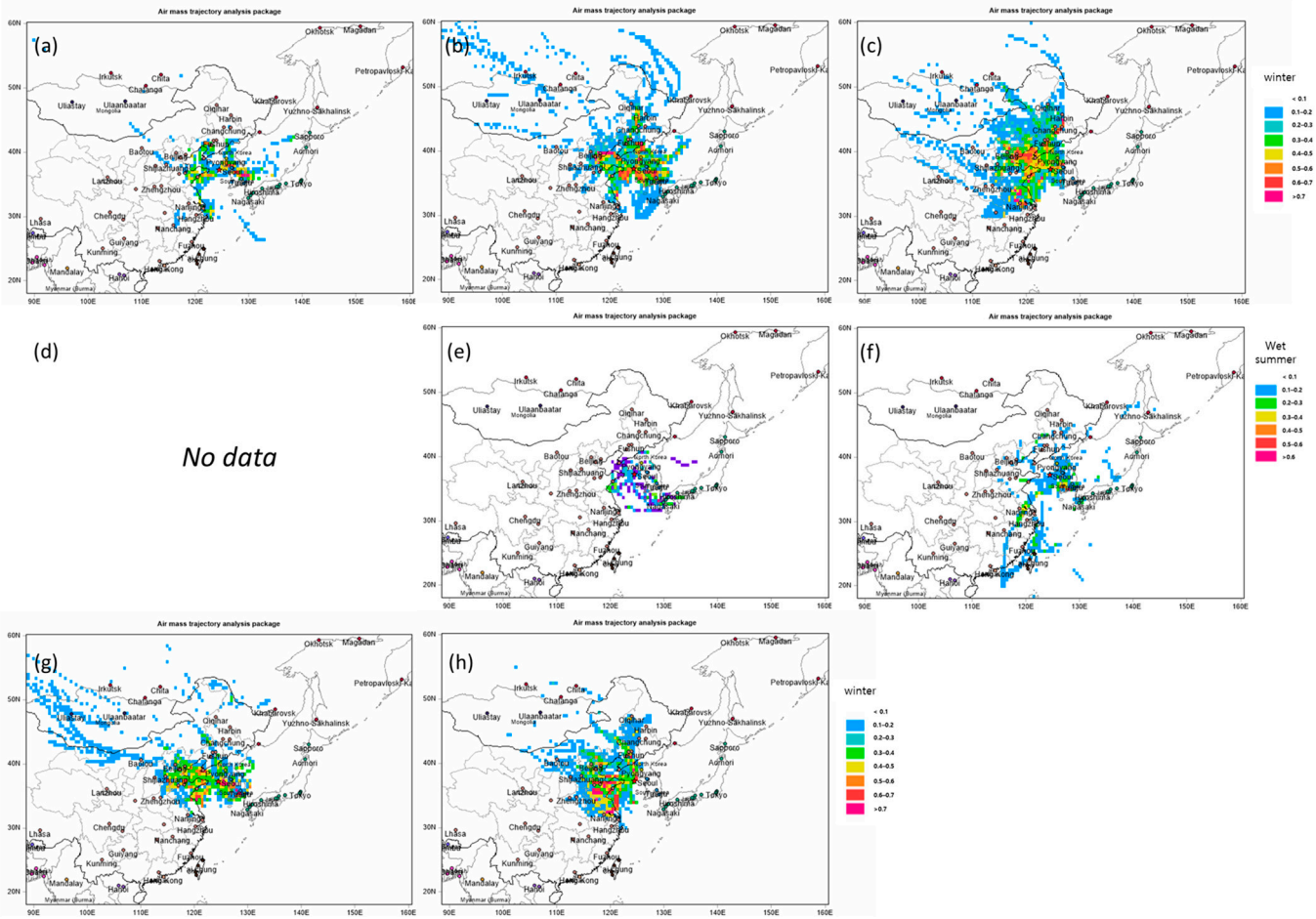

Figure 10. (**a**–**h**) Weighted potential source contribution function (WPSCF) result of 3-day back-trajectory of HYSPLIT Model for BC > 1.0 μg m^{-3} at Socheongcho Ocean Research Station (SORS) (standard).

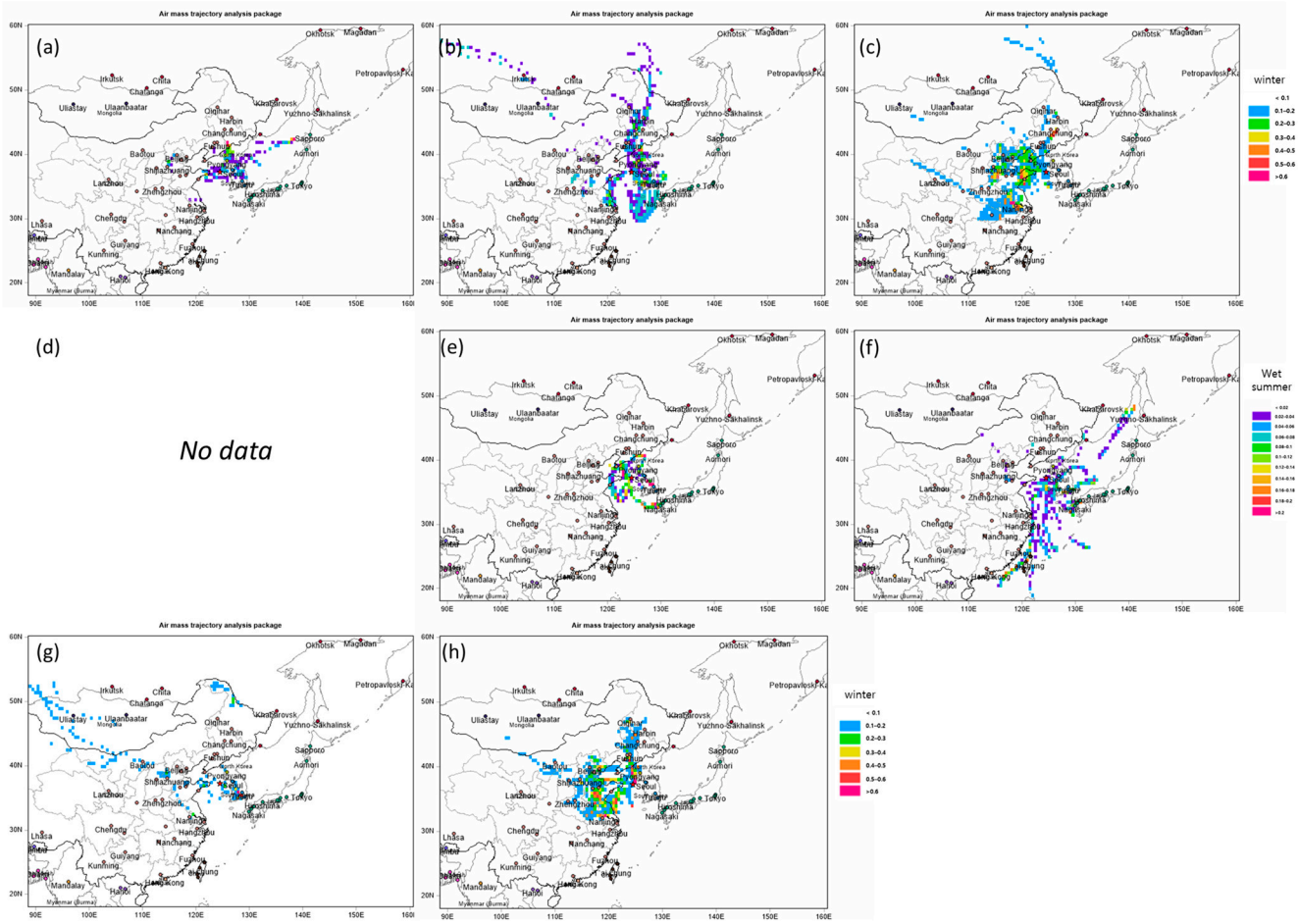

Figure 11. (**a**–**h**) Weighted potential source contribution function (WPSCF) result of 3-day back-trajectory of HYSPLIT Model for BC > 2.0 μg m^{-3} at Socheongcho Ocean Research Station (SORS) (standard).

3.3. Performance of GK-2A AODs and BC

3.3.1. Comparisons of AOD from Ground-Based and Satellite Observations and BC

The time series of the daily BC and AERONET AOD, GK-2A AOD, Terra/MODIS AOD, and Aqua/MODIS AOD (yellow circle) observations recorded at the SORS during the investigation period is presented in Figure 12. Notably, no AERONET AOD observations were available for July and September 2020, due to a heater system failure in the AERONET. Overall, the GK-2A AODs exhibited the highest concentration in July 2019 and the lowest in September 2019. The GK-2A AODs increased again in October 2019, and remained elevated until April 2020. Although the GK-2A AODs tended to be overestimated, this pattern was consistent with that of Terra, Aqua/MODIS, and AERONET. Additionally, the BC concentrations were the lowest in July 2019, and gradually increased, peaking in January 2020. A consistent distribution was observed, with the highest BC concentration in December 2020 and the lowest in July 2020. When comparing the AODs and BC, the GK-2A AODs showed the highest concentration in July 2019, while the BC concentration was at its lowest, revealing opposite trends for the AODs and BC.

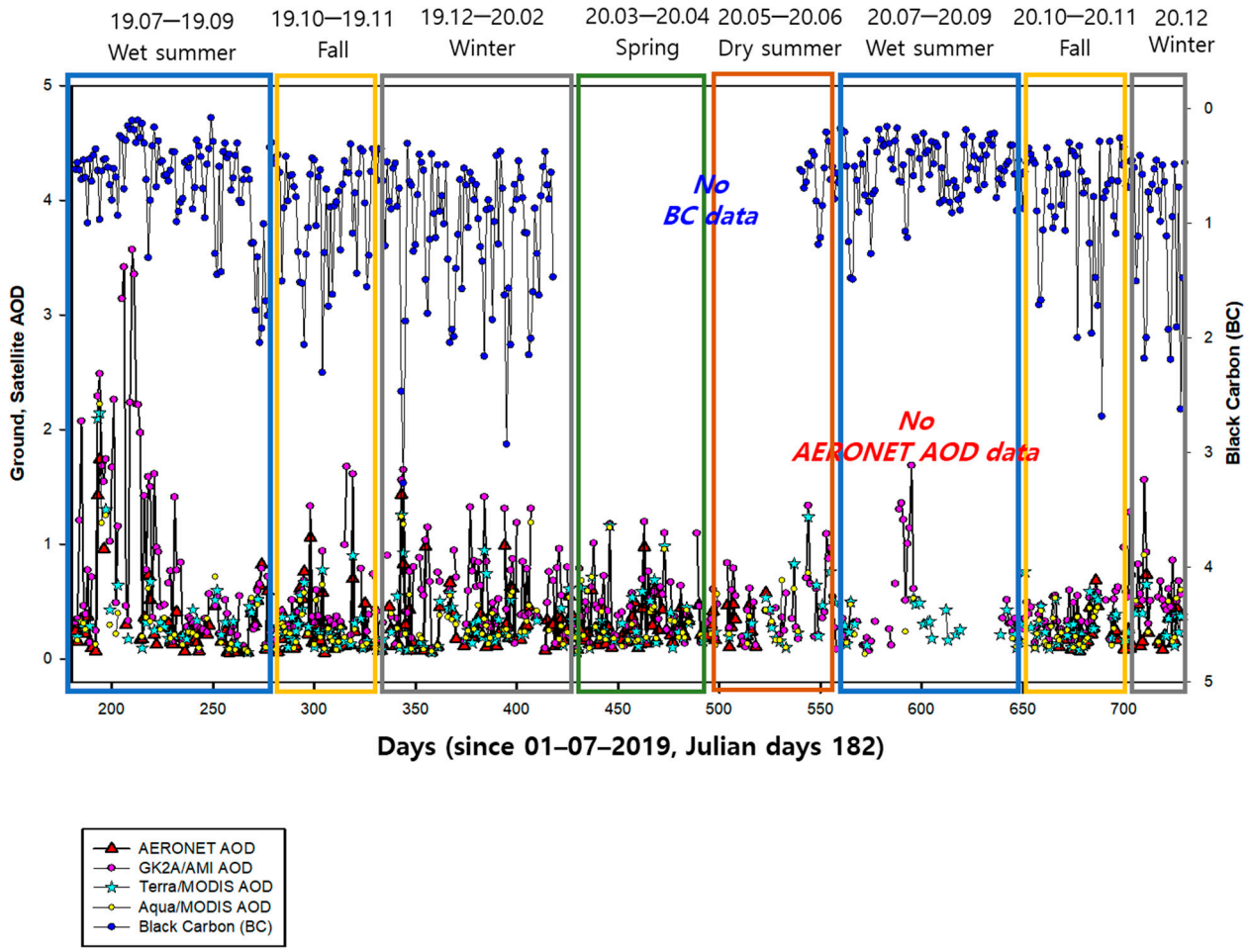

Figure 12. Time series distribution of BC (blue circle) and aerosol optical depth (AOD) from ground measurements (AERONET: red triangle) and satellites (GK-2A/AMI: pink circle, Terra/MODIS: emerald star, Aqua/MODIS: yellow circle) from July 2019 to December 2020.

Seasonal scatterplot analysis was conducted to assess aerosol loading based on aerosol properties. A scatterplot of the GK-2A AOD versus BC observations for the five seasons is presented in Figure 13. This analysis facilitated the physical examination of various aerosols and identified cluster regions with similar properties [75]. All seasons exhibited a similar relationship between BC and the GK-2A AODs in the 0–1 range. The GK-2A AODs showed a broad spread, ranging from 0 to 4 for low BC (<1.0 μg m^{-3}). This pattern was characteristic of the wet summer (yellow triangle, cluster 1), when high temperatures and humidity likely contributed to secondary effects rather than anthropogenic emissions (GK-2A AODs > BC). A similar broad spread was observed for BC, ranging from 0 to 4 for low GK-2A AODs (<1.0), which is typical of fall (orange square, cluster 2). Cluster 2 was strongly influenced by BC, which increased due to anthropogenic sources rather than meteorological factors (GK-2A AODs < BC). Cluster 3 (pink reverse triangle) showed a similar trend to cluster 2; however, when BC increased in the range of 0–3, the GK-2A AODs also tended to increase, suggesting that this pattern is characteristic of winter.

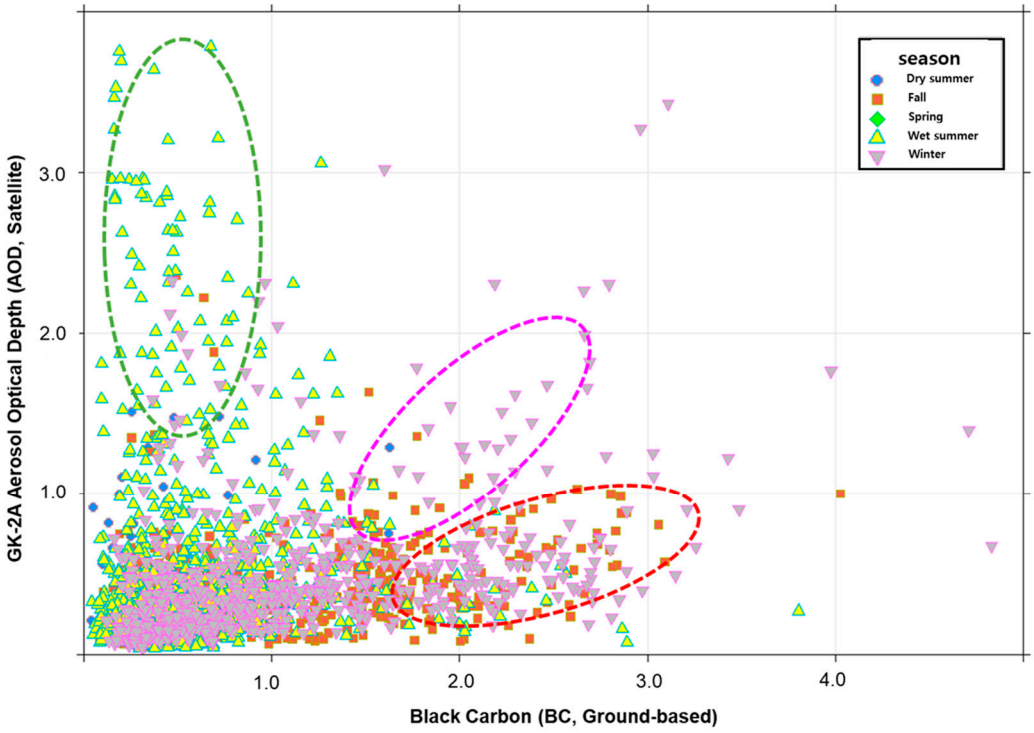

Figure 13. Scatter plot of GK-2A aerosol optical depth (AOD) and BC at Socheongcho Ocean Research Station (SORS) by season. Green triangle: wet summer (July, August), red square: fall (September, October), lavender triangle: winter (December, January, February), green rhombus: spring (March, April), and blue circle: dry summer (May, June).

3.3.2. Case Study of Seasonal Aerosol Episodes

To monitor AOD during the daytime, aerosols must be accurately detected using visible channels. For qualitative evaluation, we used true RGB imagery from the GK-2A/AMI (developed by Korea Meteorological Administration National Meteorological Satellite Center). True RGB imagery is designed to closely resemble human visual perception by using the red, green, and blue channels, the three primary colors of light. In particular, visible channels offer higher spatial resolution than infrared channels, enabling detailed observation; however, their use is limited to the daytime, as they rely on reflection components. The reflectivity of the visible channel typically exhibits high values on surfaces such as snow, ice, and clouds, but relatively low values on the Earth's surface or oceans. This characteristic allows differentiation between thin and thick clouds, as the surface roughness and light shading effects vary, even for the same material. An appropriate channel was selected to detect aerosols, and conversion to R (0.64 μg), G (0.51 + 0.86 μg), and B (0.47 μg) was performed using the reflectance of the visible channel to monitor aerosol occurrence.

- Case 1: 12–15 July 2019 (wet summer, monsoon)

The 24 h continuous measurements of GK-2A, AERONET AOD, and BC concentrations at the SORS are shown in Figure 14. This episode illustrates the general characteristics of the wet summer, with high AOD and f(RH), which is defined as the ratio of the ambient aerosol scattering coefficient at a given RH to that in dry air conditions, and low BC concentration. Increases in RH can lead to higher f(RH) and AOD values. Specifically, a decrease in PBLH can cause an increase in AOD concentration. Thus, RH and PBLH play key roles in AOD growth, demonstrating an anti-correlated temporal trend. BC was measured at 1 h intervals, while the GK-2A and AERONET AODs were measured at 10 min intervals and averaged over 1 h. From July 12 to 15, the average values of the GK-2A AOD and AERONET AOD were 2.13 and 1.68, respectively, with maximum values of 3.31 and 2.76,

respectively. The high AOD during this episode was primarily attributed to the increase in the hygroscopic growth factor with rising RH. This caused the particles to become more spherical as water vapor condensed at higher humidity, thereby enhancing the scattering coefficient. The hygroscopic properties of aerosols, due to hydrophilic particles in the lower troposphere, can influence the magnitude of aerosol radiative forcing, both at the TOA and at the surface. In contrast, low PBLH contributes to an increase in particle numbers, as aerosols are trapped in the atmosphere. Particularly in summer, pronounced turbulence further alters AOD concentrations [76].

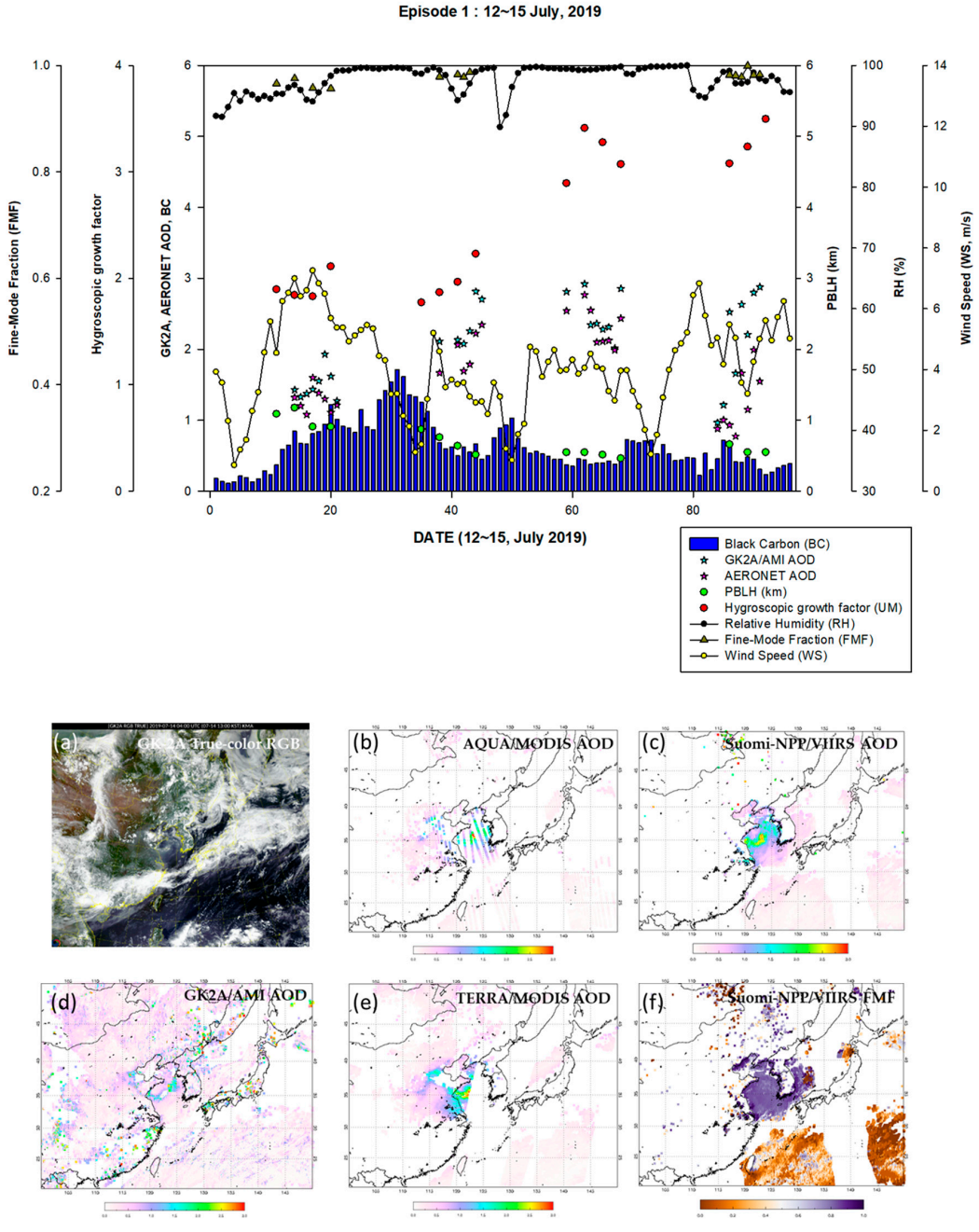

Figure 14. Time series of aerosol episode on 12–15 July 2019 and images of high-aerosol event obtained on 04:00 UTC, 14 July 2019, using (**a**) GK-2A True = RGB, (**b**) GK-2A/AMI aerosol optical depth (AOD), (**c**) Terra/MODIS AOD, (**d**) Aqua/MODIS AOD, (**e**) Suomi-NPP/VIIRS AOD, and (**f**) Suomi-NPP/VIIRS FMF.

The average BC concentration was 0.63 μg m^{-3}, with a maximum of 1.71 μg m^{-3}, suggesting that the pollutants likely originated from local sources or had minimal regional impact. Additionally, the AERONET fine-mode fraction (FMF) was close to 1.0, indicating a predominance of fine particle aerosols over coarse particles. Therefore, it was concluded that the SORS during the wet summer had a greater effect on AOD than on the primary emissions of BC. The higher precipitable water vapor (H_2O) in summer likely accelerated the hygroscopic growth of aerosols, increasing AOD values [77]. During this episode, aerosols were primarily sourced from local urban/industrial areas due to infrequent heavy winds, which likely led to the accumulation of local pollutants in a stable atmosphere [78]. Thus, this episode was characterized by conditions conducive to increased aerosol concentrations in summer, including a stable, humid atmosphere and the influx of external pollutants.

At 04:00 UTC on July 14, the true RGB imagery from the GK-2A (Figure 14a) was observed in detail over the Korean Peninsula, at a resolution of 2 km. It revealed that hazy smoke from southern China had become entangled with clouds, and remained over the Yellow Sea. Additionally, a comparative analysis of the AODs from each satellite in the East Asia region showed that the GK-2A AOD (Figure 14b) at the SORS was ≥2.0 over the Yellow Sea. The Terra·Aqua/MODIS and Suomi-NPP/VIIRS AODs exhibited similar values (Figure 14c,d). Furthermore, the Suomi-NPP/VIIRS (Figure 14e) had a wider swath (~3000 km) [45] than the Terra·Aqua/MODIS. Despite being a polar-orbiting satellite, its concentration at the SORS could be qualitatively compared. The FMF (Figure 14f) of the Suomi-NPP/VIIRS was ≥0.8, and its AE was ≥1.25, indicating that small particles, rather than large ones, were likely responsible for the high AOD. However, the GK-2A failed to accurately detect the AOD over the Yellow Sea, likely due to excessive cloud masking. In comparison to polar-orbiting satellites, cloud masking is typically applied more rigorously to improve accuracy.

- Case 2: October 30–2 November 2019 (fall, post-monsoon season)

Most episodes occurring in the fall exhibited low AOD concentrations, but high BC concentrations. Since BC can influence the optical properties of the atmosphere, the diurnal variation in BC and AOD during this episode was analyzed to assess any correlation (Figure 15). The BC concentration steadily increased from October 30–31, while the GK-2A and AERONET AODs showed low concentrations. Specifically, the PBLH was <1 km due to the stable background atmosphere and minimal AOD range (0.00–0.50), indicating a stable condition with minimal perturbations. This stability allowed the particles to remain in the atmosphere longer, facilitating their accumulation [45]. Additionally, the FMF was <0.5, suggesting that the pollutants were primarily composed of large particles rather than small ones. Thus, the primary pollutant during this episode was introduced and accumulated in the SORS, rather than secondary organic matter aerosols. As autumn light diminishes, photochemical reactions experience a reduction in energy, leading to fewer secondary aerosol particles [79]. The peak in BC during this episode appears to result from a combination of atmospheric boundary layer characteristics and anthropogenic influences. These results suggest that particles formed through gas-particle conversion in the fall significantly decreased, while coarse-mode aerosols increased due to primary inflow. Furthermore, at 04:00 UTC on October 31, the true RGB imagery from the GK-2A (Figure 15a) showed a white cloud of smoke covering the entire Yellow Sea. The AOD from each satellite ranged between 0.5 and 1, and was centered on the SORS region, as indicated by the detailed analysis above. The GK-2A AODs (Figure 15b) were similar to those of the Terra·Aqua/MODIS (Figure 15c,d), suggesting high accuracy for the GK-2A. The Suomi-NPP/VIIRS (Figure 15e,f) was not observed in East Asia at 04:00 UTC. The GK-2A AOD

concentration distribution exhibited a vortex shape around the SORS, observed from the satellite as aerosol particles remaining due to the weakening of the wind speed, WS.

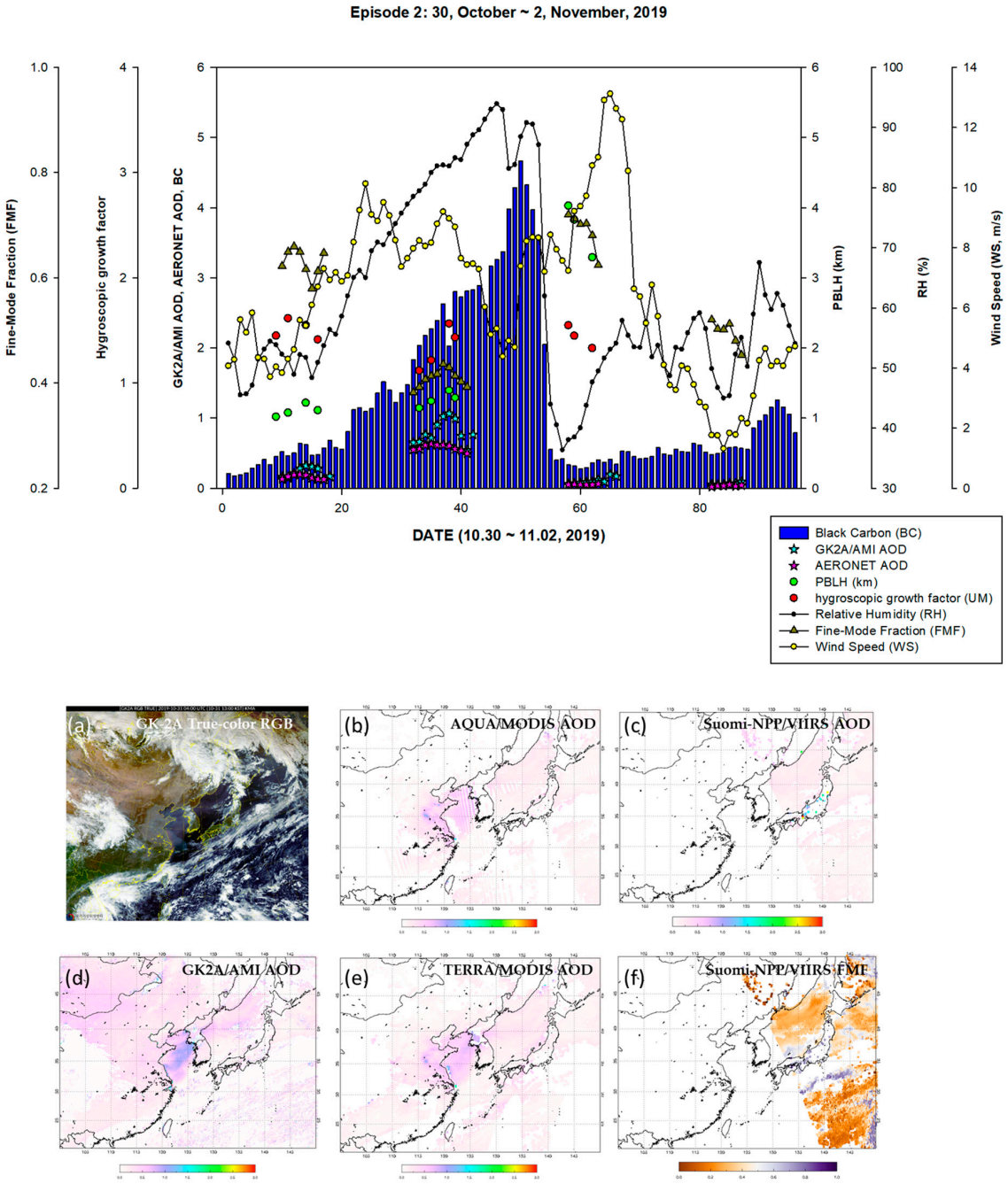

Figure 15. Time series of aerosol episode on 30 October–2 November 2019 and images of fall aerosol event obtained at 04:00 UTC on 30 October 2019, using (**a**) GK-2A True RGB, (**b**) GK-2A/AMI AOD, (**c**) Terra/MODIS AOD, (**d**) Aqua/MODIS AOD, (**e**) Suomi-NPP/VIIRS AOD, and (**f**) Suomi-NPP/VIIRS FMF.

- Case 3: 7–10 December 2019 (winter)

On December 7 (Figure 16), a high AOD (>0.5) was observed in the morning, which gradually decreased, increased at noon, and then decreased again. This pattern could be attributed to the diffusion process associated with increasing RH and temperature throughout the day. As the GK-2A and AERONET AODs increased, both the RH and the hygroscopic growth factor (>2.0) temporarily increased, and the FMF was approximately 0.9, indicating the predominance of small particles. Moreover, the BC concentration began

to increase during the daytime and after sunset, due to the decrease in temperature and PBLH, which restricted the dispersion of BC on December 9. Under similar conditions, high BC (5.78 μg m^{-3}) was observed in the evening due to a steep reduction in WS. On December 10, the trend of increasing GK-2A AODs and AERONET AODs over time was consistent, with the hygroscopic growth factor remaining high, at ≥2.0. However, as WS rapidly decreased, BC increased as pollutants accumulated, and the FMF was <0.7, suggesting that BC had a greater influence than AOD. Thus, the simultaneous increases in the GK-2A AOD and BC led to the accumulation of both coarse- and fine-mode particles.

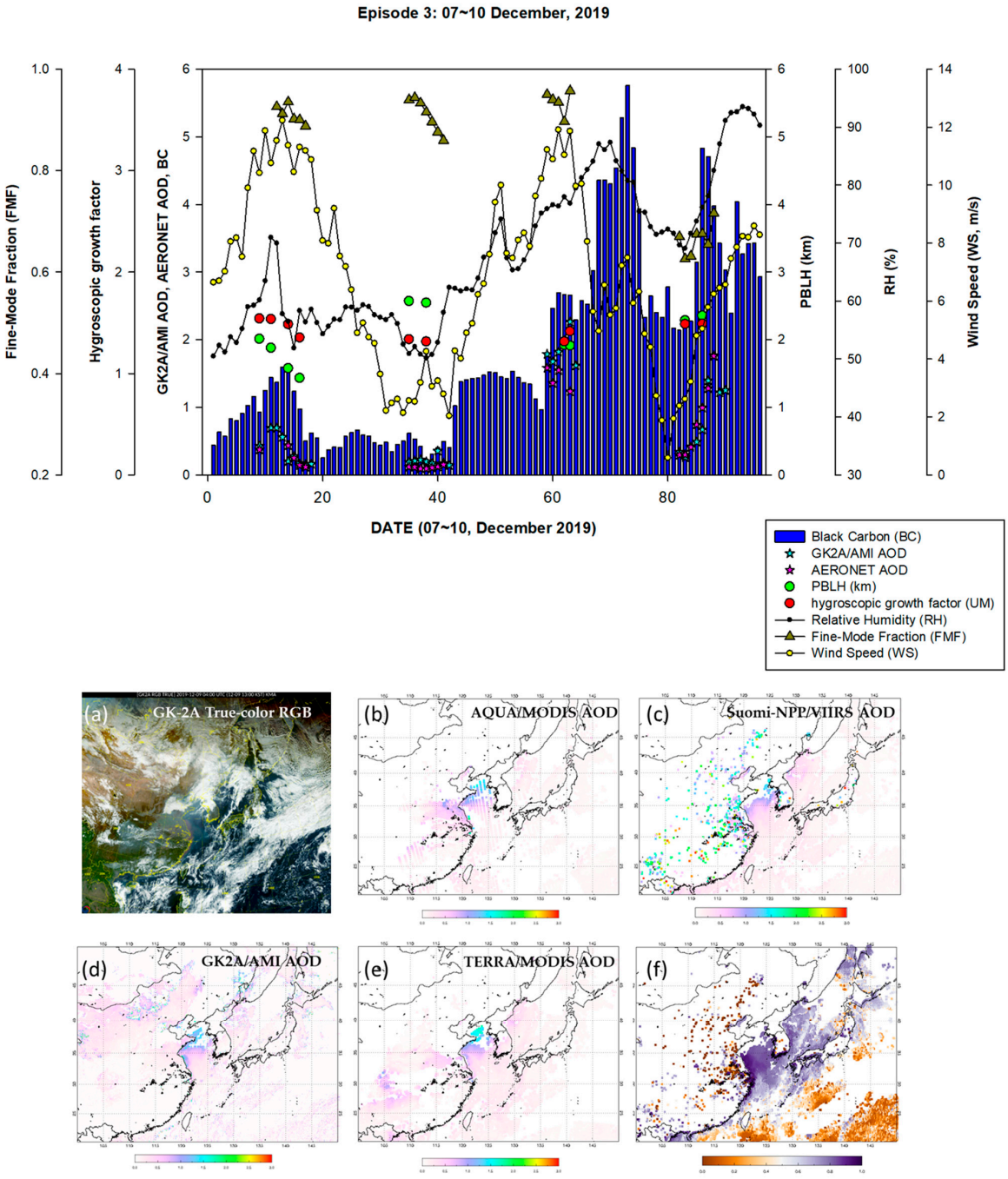

Figure 16. Time series of aerosol episode on 7–10 December 2019 and images of winter aerosol event obtained at 04:00 UTC, on 9 December 2019, using (**a**) GK-2A True RGB, (**b**) GK-2A/AMI aerosol optical depth (AOD), (**c**) Terra/MODIS AOD, (**d**) Aqua/MODIS AOD, (**e**) Suomi-NPP/VIIRS AOD, and (**f**) Suomi-NPP/VIIRS FMF.

The atmospheric conditions in winter were dry and cold, with strong winds that facilitated aerosol dispersion. However, the hygroscopic growth effect of aerosol particles was weak due to lower RH, which changed over a wide range. The diurnal pattern was most pronounced during the winter. At 04:00 UTC on December 9, the RGB of the GK-2A (Figure 16a) showed smoke rising between clouds centered on the SORS, with turbidity along the coastline of the Yellow Sea appearing red. Additionally, the AOD analysis from each satellite indicated that the GK-2A AOD (Figure 16b) and VIIRS (Figure 16e) showed values $\geq$0.8, while the Terra·Aqua/MODIS (Figure 16c,d) showed values $\geq$1.0. This suggested that the pollution from southern China passed through the Yellow Sea and remained near the SORS, resulting in high aerosol concentrations. In particular, the FMF (Figure 16f) for the Suomi-NPP/VIIRS showed a high value (>0.8) over the ocean and a low value (<0.4) over land, indicating that fine particles were distributed over the ocean, while large particles originating from pollutants were found primarily over land. Therefore, both AOD and BC concentrations increased simultaneously at the SORS in winter, with both large and small particles coexisting, as observed through ground-based and satellite data. The primary pollutant source was carried by wind, with secondary reactions occurring over the ocean.

3.3.3. Influence of Meteorological Parameters

Figure 17 shows the SHapley Additive exPlanations-based feature significance results for the GK-2A AODs and BC during the analysis period. Each point represents the contribution of each feature to the GK-2A AODs and BC over the analyzed period. For the GK-2A AODs (Figure 17a), the RH feature was dominant, with high values. Atmospheric humidity influences the size and properties of aerosols, particularly promoting aerosol scattering due to the hygroscopic growth of particles as RH increases [75,80]. As RH increases, aerosol scattering rises, leading to an increase in AOD. Temperature also played an important role, with higher temperatures during the wet summer (especially in July 2019) corresponding to higher AOD values at the SORS. When temperature increases, local winds produce thermal differences due to uneven heating, which enhances turbulence, lifting dust into the air and raising aerosol concentrations. Additionally, increased RH levels in the wet summer were linked to higher temperatures, which resulted in substantial evaporation from the nearby Yellow Sea, raising atmospheric water vapor levels. Specifically, the SORS, located on the coast, exhibited high AOD values, likely due to elevated evaporation rates.

The impact of meteorological factors on the GK-2A AOD at the SORS was ranked as follows: RH > evaporation (H_2O) > temperature > hygroscopic growth factor > AERONET 412 nm AOD [81]. For BC (Figure 17b), the $PM_{2.5}$ feature had the most significant influence, with concentrations of both $PM_{2.5}$ and BC increasing during fall and winter under northwesterly winds. BC, a tracer of primary anthropogenic emissions [82], is associated with the transport of primary air pollutants produced by combustion processes from surrounding areas [83]. As observed in the trajectory analysis, BC is generated as a primary emission, and the wind direction indicates the source region. Feature analysis showed that wind direction strongly influenced BC concentration, particularly in the northwest direction. BC, a byproduct of the incomplete oxidation of CO, is a key characteristic of this pollutant. Notably, large increases in CO were observed during the cold season, suggesting that domestic coal/biofuel combustion contributed to heating. CO concentrations significantly increased in winter due to the frequent shifting of air masses from clean continental interiors to heavily polluted urban plumes, particularly during the heating period (normally from November to March in northern China). The impact of meteorological factors on BC at the SORS was ranked as follows: $PM_{2.5}$ > wind direction > CO > AERONET 870 nm, 1020 AOD nm.

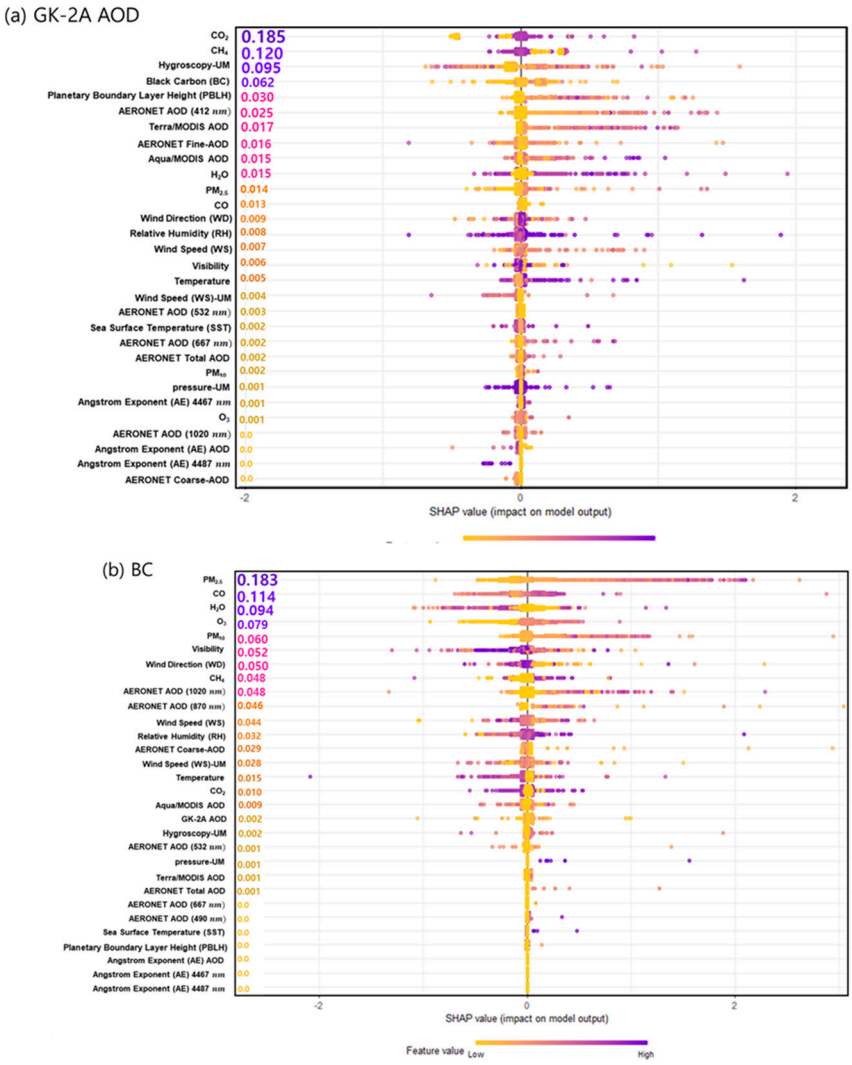

Figure 17. SHapley Additive exPlanations-based feature importance results for (**a**) GK-2A aerosol optical depth (AOD) and (**b**) black carbon (BC) during analysis period.

A heatmap-based analysis is shown in Figure 18. To further investigate the factors influencing each season, a hierarchical cluster analysis was performed according to seasonal (Figure 18a), monthly (Figure 18b), optical property, gaseous constituent, and meteorological parameters [84]. The categorized groups aligned with the known seasonal characteristics of these parameters. The dry summer group exhibited a high correlation with AE ($\alpha_{440-670}$), RH, H_2O (evaporation), Terra·Aqua/MODIS AOD, and O_3, which predominantly contributed to the formation of hygroscopic aerosols. AE ($\alpha_{440-670}$) reflects significant spectral variation in aerosol size distribution, particularly for accumulation-mode aerosols [33,85]. This factor is believed to have a more pronounced effect on fine particles than coarse particles during dry summer. Additionally, the strong influence of LEO satellites in dry summers indicates the high accuracy of polar-orbiting satellites in detecting fine-mode aerosol particles. Similarly, during wet summer, notable features in the GK-2A AOD, AE ($\alpha_{440-870}$), and hygroscopic growth factor were observed. Specifically, AE ($\alpha_{440-870}$) measures the relative dominance of fine aerosols over coarse aerosols, with large values of $\alpha_{440-870}$ indicating a higher ratio of small to large particles. Like dry summer, the aerosol composition was predominantly fine-mode particles.

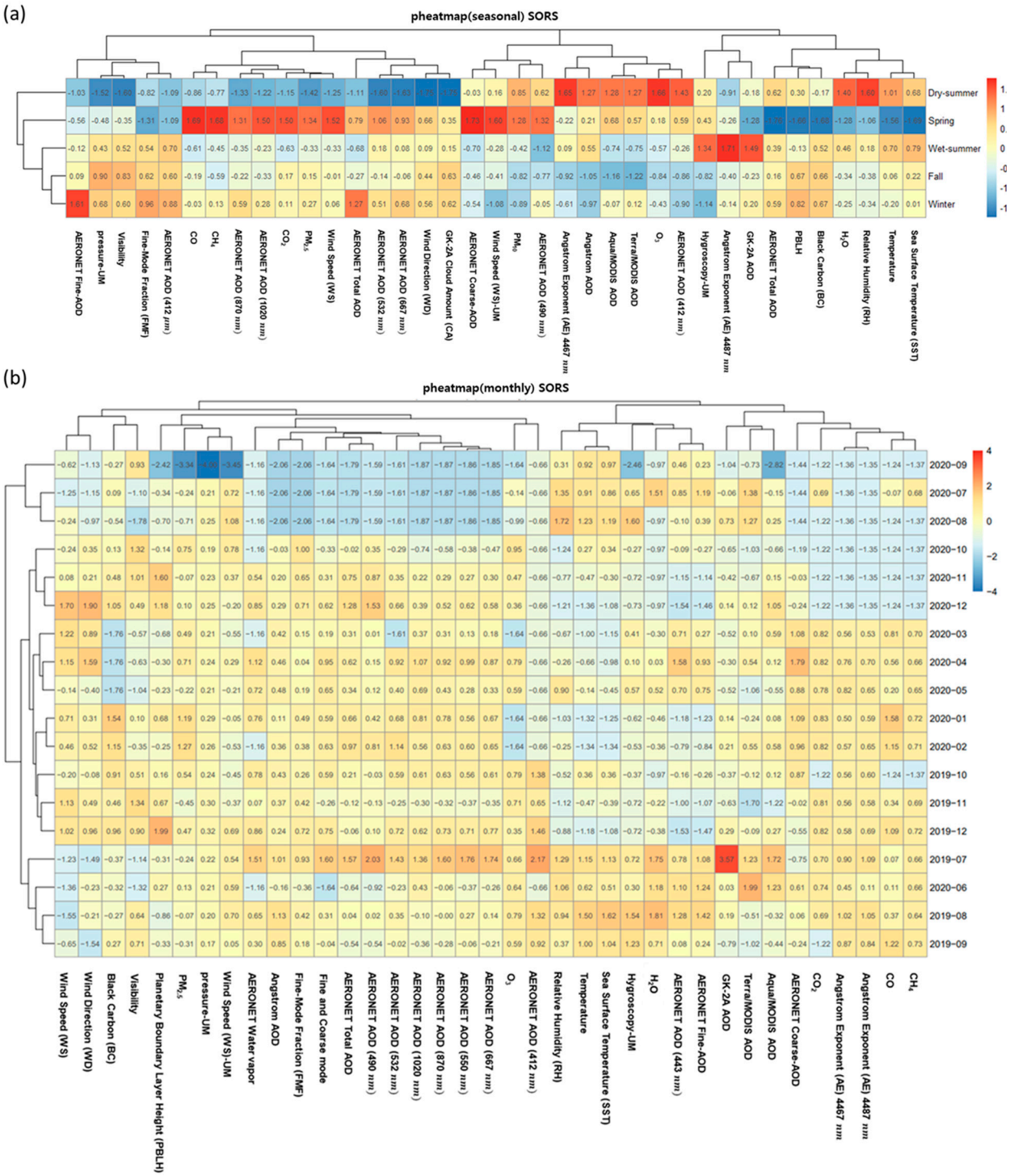

Figure 18. Results for PHEATMAP-based feature importance analysis by (**a**) season and (**b**) month.

As confirmed in Section 3.3.2, the GK-2A AODs reached the highest concentration in July 2019 during the analysis period. Aerosols, which contained significant evaporation from the dry summer, showed that their hygroscopic growth was maximized during the wet summer, influenced by various weather conditions over time. In contrast, in the fall (three groups), BC, rather than aerosol optical properties, emerged as the primary influencing factor. For gaseous substances, CH_4 and CO were identified as important factors, and were considered primary pollutant sources, alongside BC. These pollutants, produced during incomplete anthropogenic combustion processes, serve as convenient indicators of anthropogenic influence on air masses [86].

Winter (four groups) exhibited both BC and AOD effects. The most notable feature was the highest concentration of total AOD observed for AERONET, with the fine mode having the greatest influence. The FMF of AERONET was the highest, with its most prominent characteristic observed at 412 nm, the shortest wavelength. This suggests that smaller aerosol particles scatter more at shorter wavelengths. The spectral dependence of AOD values in the UV-VIS range highlights the significance of fine-mode aerosols in scattering processes, especially during winter [87]. Additionally, BC and CH_4 concentrations were highest in winter, indicating the coexistence of aerosol scattering and absorption due to primary combustion.

Spring, the final group, could not be confirmed due to the unavailability of BC data; however, AOD values were high in the coarse mode of AERONET, which contrasted with winter. Specifically, the AOD was elevated at 870 and 1020 nm, the longest wavelengths of AERONET, similarly to the phenomenon observed when large aerosols, such as yellow dust, are present. The gradient in spectral variability between the AODs at shorter and longer wavelengths across seasons indicated an asymmetric distribution of aerosol sizes, highlighting the seasonal shift in the dominance of fine- and coarse-mode aerosols [88]. Additionally, the high values of $PM_{2.5}$ and PM_{10} provided further evidence of the presence of large-particle aerosols on the ground.

4. Conclusions

The AODs and BC aerosol mass concentrations were measured at the SORS, a national monitoring station that tracks the background concentration of fine dust generated in Korea, as well as long-range external air pollutants, such as those from China. The main conclusions of the study are summarized as follows:

- The GK-2A AOD retrieval algorithm utilized five-channel reflectance (0.47, 0.51, 0.64, 0.86, and 1.61 μm) to calculate path radiances at three visible channels (0.47, 0.64, and 0.86 μm), enabling the selection of appropriate aerosol optical property models and aerosol loading. In particular, it is novel that it included more accurate cloud detection of AMI and bright surface masking via its SWIR and IR channels. Also, it reduced seasonal temperature differences by using the average aerosol background field for 30 days before observation. Therefore, it has the advantage of being able to quickly monitor aerosol movement over the Korean Peninsula at 2 min intervals, with a high resolution of 2 km.
- The GK-2A AOD algorithm demonstrated high accuracy, with a strong correlation (R^2 = 0.85, slope = 0.12) when compared to AERONET. Its performance was comparable to that of the MODIS (Terra: R^2 = 0.86, slope = 0.78; Aqua: R^2 = 0.83, slope = 0.76).
- During the wet summer, the GK-2A AOD values were approximately double (0.63) those observed in winter (0.31) at the SORS. Similarly, the BC mass concentrations ranged from 2 μg·m^{-3} during the wet summer monsoon to 6 μg m^{-3} in winter and the post-monsoon season.
- Based on WPSCF model analysis and meteorological data, the AOD and BC concentrations were influenced by long-distance transport from China. Lower BC concentrations during the monsoon season were attributed to wet removal near the surface, while higher concentrations in winter and post-monsoon periods were associated with shallow boundary layers, low wind speeds, and northwesterly/northerly winds facilitating pollutant transport. In contrast, the GK-2A AOD values increased during the monsoon, due to water vapor transport from the southwest, south, and southeast winds. The AOD further increased when air stagnated over the YRD region, including Nanjing and Hangzhou.

- The GK-2A AOD values were primarily influenced by RH, the hygroscopic growth factor, and H_2O (water vapor), whereas BC concentrations were increased, along with $PM_{2.5}$ and CO levels, during fall and winter
- Seasonal analysis revealed that pollutant diffusion was limited during winter, with AOD and BC concentrations increasing due to pollutants lingering near the surface. This was attributed to lower planetary boundary layer heights (PBLHs) and minimal rainfall, allowing aerosols to accumulate. During wet summer, high RH and significant water vapor content promoted hygroscopic aerosol growth, increasing AOD values. In spring, the inflow of large particles, such as yellow dust, enhanced scattering properties, thereby raising AOD values.
- The source of BC concentrations at the SORS was influenced by meteorological factors. Long-range transport via northwesterly winds increased CO levels, while local emissions were linked to elevated $PM_{2.5}$, PM_{10}, and RH.
- The analysis of the GK-2A AOD and BC aerosol mass concentration data confirmed that the SORS is impacted by combustion products from both local and remote sources. However, extended observation periods are necessary to establish definitive conclusions and fully understand variations in AOD and BC levels. Future studies will expand the network of monitoring sites and conduct long-term continuous measurements for a more comprehensive analysis.

Author Contributions: Conceptualization, S.A. and M.L.; methodology: S.A. and H.-S.K.; software: S.A.; validation: S.A. and H.-S.K.; formal analysis: S.A. and M.L.; investigation: S.A.; resources: S.A.; data curation: S.A. and J.-Y.J.; writing—original draft preparation: S.A.; writing—review and editing: M.L. and E.-h.S.; visualization: S.A.; supervision: M.L.; project administration: E.-h.S. All authors have read and agreed to the published version of the manuscript.

Funding: This research was supported by the project "The Technical Development on Weather Forecast Support and Convergence Service Using Meteorological Satellites", NMSC/KMA (KMA2020-00121), and by the Korea Institute of Marine Science and Technology Promotion (KIMST), funded by the Ministry of Oceans and Fisheries (20210607, "Establishment of the Ocean Research Station in the Jurisdiction Zone and Convergence Research").

Data Availability Statement: The data presented in this study are available upon request from the corresponding author, subject to restrictions related to privacy or ethical considerations.

Conflicts of Interest: The authors declare no conflicts of interest.

References

1. Zhang, B.; Chen, L.; Liu, M.; Zhao, J. The effect of aerosols on climate change and society. *J. Geosci. Environ. Prot.* **2020**, *8*, 55. [CrossRef]
2. Berndes, G.; Abt, B.; Asikainen, A.; Cowie, A.; Dale, V.; Egnell, G.; Yeh, S. Forest biomass, carbon neutrality, and climate change mitigation. *From Sci. Policy* **2016**, *3*, 1–27.
3. Andreae, M.O.; Gelencsér, A. Black carbon or brown carbon? The nature of light-absorbing carbonaceous aerosols. *Atmos. Chem. Phys.* **2006**, *6*, 3131–3148. [CrossRef]
4. Haywood, J.; Boucher, O. Estimates of the direct and indirect radiative forcing due to tropospheric aerosols: A review. *Rev. Geophys.* **2000**, *38*, 513–543. [CrossRef]
5. Roeckner, E.; Stier, P.; Feichter, J.; Kloster, S.; Esch, M.; Fischer-Bruns, I. Impact of carbonaceous aerosol emissions on regional climate change. *Clim. Dyn.* **2006**, *27*, 553–571. [CrossRef]
6. Lim, S.; Lee, M.; Yoo, H.J. Size distributions, mixing state, and morphology of refractory black carbon in an urban atmosphere of Northeast Asia during summer. *Sci. Total Environ.* **2023**, *856*, 158436. [CrossRef]
7. Li, N.; Chartier, R.; Li, Y.; Liu, Z.; Li, N.; Chang, J.; Xu, C. Measuring and modeling of residential black carbon concentrations in two megacities, China. *Build. Environ.* **2024**, *257*, 111558. [CrossRef]
8. Park, D.; Kang, K.; Na, H.; Lee, J.; Kim, S.; Kim, T. Measurement of black carbon exposure in urban classrooms during rush hours. *Atmos. Pollut. Res.* **2024**, *15*, 102233. [CrossRef]

9. Li, Y.; Zhang, J.; Duan, Q.; Kong, X.; Wang, H. Temporal evolution and source apportionment of BC aerosols during autumn in the grassland of Ordos, China. *Meteorol. Appl.* **2024**, *31*, e2172. [CrossRef]
10. Mann, G.W.; Carslaw, K.S.; Reddington, C.L.; Pringle, K.J.; Schulz, M.; Asmi, A.; Henzing, J.S. Intercomparison and evaluation of global aerosol microphysical properties among AeroCom models of a range of complexity. *Atmos. Chem. Phys.* **2014**, *14*, 4679–4713. [CrossRef]
11. Croft, B.; Lohmann, U.; von Salzen, K. Black carbon ageing in the Canadian Centre for Climate Modelling and Analysis atmospheric general circulation model. *Atmos. Chem. Phys.* **2005**, *5*, 1931–1949. [CrossRef]
12. Lohmann, U.; Feichter, J. Global indirect aerosol effects: A review. *Atmos. Chem. Phys.* **2005**, *5*, 715–737. [CrossRef]
13. Wang, D.; Zhang, F.; Yang, S.; Xia, N.; Ariken, M. Exploring the spatial-temporal characteristics of the aerosol optical depth (AOD) in Central Asia based on the moderate resolution imaging spectroradiometer (MODIS). *Environ. Monit. Assess.* **2020**, *192*, 1–15. [CrossRef]
14. Wang, J.; Christopher, S.A. Intercomparison between satellite-derived aerosol optical thickness and PM2.5 mass: Implications for air quality studies. *Geophys. Res. Lett.* **2003**, *30*, 2095. [CrossRef]
15. Remer, L.A.; Mattoo, S.; Levy, R.C.; Munchak, L.A. MODIS 3 km aerosol product: Algorithm and global perspective. *Atmos. Meas. Tech.* **2013**, *6*, 1829–1844. [CrossRef]
16. Huang, J.; Kondragunta, S.; Laszlo, I.; Liu, H.; Remer, L.A.; Zhang, H.; Superczynski, S.; Ciren, P.; Holben, B.N.; Petrenko, M. Validation and expected error estimation of Suomi-NPP VIIRS aerosol optical thickness and Ångström exponent with AERONET. *J. Geophys. Res. Atmos.* **2016**, *121*, 7139–7160. [CrossRef]
17. Liu, H.; Remer, L.A.; Huang, J.; Huang, H.C.; Kondragunta, S.; Laszlo, I.; Oo, M.; Jackson, J.M. Preliminary evaluation of S-NPP VIIRS aerosol optical thickness. *J. Geophys. Res. Atmos.* **2014**, *119*, 3942–3962. [CrossRef]
18. Nakajima, T.; Nakajima, T.Y.; Higurashi, A.; Sano, I.; Takamura, T.; Ishida, H.; Schutgens, N. A study of aerosol and cloud information retrievals from CAI imager on board GOSAT satellite. *J. Remote Sens. Soc. Jpn.* **2008**, *28*, 178–189. [CrossRef]
19. Ahn, S.; Kim, H.S.; Byon, J.Y.; Lim, H. Improving dust aerosol optical depth (DAOD) retrieval from the GEOKOMPSAT-2A (GK-2A) satellite for daytime and nighttime monitoring. *Sensors* **2024**, *24*, 1490. [CrossRef]
20. Song, S.; Kang, Y.; Im, J. Enhanced continuous aerosol optical depth (AOD) estimation using geostationary satellite data: Focusing on nighttime AOD over East Asia. *arXiv* **2024**, arXiv:2405.13334. [CrossRef]
21. Kim, M.; Kim, J.; Lim, H.; Lee, S.; Cho, Y.; Lee, Y.G.; Lee, K. Aerosol optical depth data fusion with Geostationary Korea Multi-Purpose Satellite (GEO-KOMPSAT-2) instruments GEMS, AMI, and GOCI-II: Statistical and deep neural network methods. *Atmos. Meas. Tech.* **2024**, *17*, 4317–4335. [CrossRef]
22. Lee, S.; Choi, J. Daytime cloud detection algorithm based on a multitemporal dataset for GK-2A imagery. *Remote Sens.* **2021**, *13*, 3215. [CrossRef]
23. Jee, J.B.; Lee, K.T.; Lee, K.H.; Zo, I.S. Development of GK-2A AMI aerosol detection algorithm in the East-Asia region using Himawari-8 AHI data. *Asia-Pac. J. Atmos. Sci.* **2020**, *56*, 207–223. [CrossRef]
24. Min, Y.; Jeong, J.Y.; Min, I.K.; Kim, Y.S.; Shim, J.S.; Do, K. Enhancement of wave radar observation data quality at the Socheongcho Ocean Research Station. *J. Coast. Res.* **2018**, *85*, 571–575. [CrossRef]
25. Petzold, A.; Schönlinner, M. Multi-angle absorption photometry—A new method for the measurement of aerosol light absorption and atmospheric black carbon. *J. Aerosol Sci.* **2004**, *35*, 421–441. [CrossRef]
26. Lee, D.; Jeong, J.Y.; Jang, H.K.; Min, J.O.; Kim, M.J.; Youn, S.H.; Lee, T.; Lee, S.H. Comparison of particulate organic carbon to Chlorophyll-a ratio based on the ocean color satellite data at the Ieodo and Socheongcho ocean research stations. *J. Coast. Res.* **2019**, *90*, 267–271. [CrossRef]
27. Petzold, A.; Schloesser, H.; Sheridan, P.J.; Arnott, W.P.; Ogren, J.A.; Virkkula, A. Evaluation of multiangle absorption photometry for measuring aerosol light absorption. *Aerosol Sci. Technol.* **2005**, *39*, 40–51. [CrossRef]
28. Holben, B.N.; Eck, T.F.; Slutsker, I.A.; Tanre, D.; Buis, J.P.; Setzer, A.; Vermote, E.; Reagan, J.A.; Kaufman, Y.J.; Nakajima, T.; et al. AERONET—A federated instrument network and data archive for aerosol characterization. *Remote Sens. Environ.* **1998**, *66*, 1–16. [CrossRef]
29. Choi, M.; Kim, J.; Lee, J.; Kim, M.; Park, Y.J.; Holben, B.; Eck, T.F.; Li, Z.; Song, C.H. GOCI Yonsei aerosol retrieval version 2 products: An improved algorithm and error analysis with uncertainty estimation from 5-year validation over East Asia. *Atmos. Meas. Tech.* **2018**, *11*, 385–408. [CrossRef]
30. Ahn, C.; Torres, O.; Jethva, H. Assessment of OMI near-UV aerosol optical depth over land. *J. Geophys. Res. Atmos.* **2014**, *119*, 2457–2473. [CrossRef]
31. Dubovik, O.; Holben, B.N.; Lapyonok, T.; Sinyuk, A.; Mishchenko, M.I.; Yang, P.; Slutsker, I. Non-spherical aerosol retrieval method employing light scattering by spheroids. *Geophys. Res. Lett.* **2002**, *29*, 54-1–54-4. [CrossRef]

32. Giles, D.M.; Sinyuk, A.; Sorokin, M.G.; Schafer, J.S.; Smirnov, A.; Slutsker, I.; Eck, T.F.; Holben, B.N.; Lewis, J.R.; Campbell, J.R.; et al. Advancements in the aerosol robotic network (AERONET) Version 3 database—Automated near-real-time quality control algorithm with improved cloud screening for sun photometer aerosol optical depth (AOD) measurements. *Atmos. Meas. Tech.* **2019**, *12*, 169–209. [CrossRef]
33. Eck, T.F.; Holben, B.N.; Reid, J.S.; Dubovik, O.; Smirnov, A.; O'Neill, N.T.; Slutsker, I.; Kinne, S. Wavelength dependence of the optical depth of biomass burning, urban, and desert dust aerosols. *J. Geophys. Res.* **1999**, *104*, 31333–31349. [CrossRef]
34. Deaconu, L.T.; Mereuță, A.; Radovici, A.; Ștefănie, H.I.; Botezan, C.; Ajtai, N. Consistency of aerosol optical properties between MODIS satellite retrievals and AERONET over a 14-year period in Central–East Europe. *Remote Sens.* **2024**, *16*, 1677. [CrossRef]
35. Ștefănie, H.I.; Radovici, A.; Mereuță, A.; Arghiuș, V.; Cămărășan, H.; Costin, D.; Ajtai, N. Variation of aerosol optical properties over Cluj-Napoca, Romania, based on 10 years of AERONET data and MODIS MAIAC AOD product. *Remote Sens.* **2023**, *15*, 3072. [CrossRef]
36. Isik, A.G.; Aslanoğlu, S.Y.; Güllü, G. Long-term evaluation of aerosol optical properties in the Levantine region: A comparative analysis of AERONET and Aqua/MODIS. *Remote Sens.* **2024**, *16*, 2651. [CrossRef]
37. Kaskaoutis, D.G.; Kambezidis, H.D.; Hatzianastassiou, N.; Kosmopoulos, P.G.; Badarinath, K.V.S. Aerosol climatology: On the discrimination of aerosol types over four AERONET sites. *Atmos. Chem. Phys. Discuss.* **2007**, *7*, 6357–6411. [CrossRef]
38. Kaskaoutis, D.G.; Badarinath, K.V.S.; Kumar Kharol, S.; Rani Sharma, A.; Kambezidis, H.D. Variations in the aerosol optical properties and types over the tropical urban site of Hyderabad, India. *J. Geophys. Res. Atmos.* **2009**, *114*, D22. [CrossRef]
39. Maity, A.; Maithani, S.; Pradhan, M. Cavity ring-down spectroscopy: Recent technological advances and applications. *Mol. Laser Spectrosc.* **2020**, 83–120. [CrossRef]
40. Ahn, S.; Jee, J.B.; Lee, K.T.; Oh, H.J. Enhanced accuracy of airborne volcanic ash detection using the GEOKOMPSAT-2A satellite. *Sensors* **2021**, *21*, 1359. [CrossRef]
41. Gupta, P.; Levy, R.C.; Mattoo, S.; Remer, L.A.; Munchak, L.A. A surface reflectance scheme for retrieving aerosol optical depth over urban surfaces in MODIS Dark Target retrieval algorithm. *Atmos. Meas. Tech.* **2016**, *9*, 3293–3308. [CrossRef]
42. Lyapustin, A.; Wang, Y.; Korkin, S.; Huang, D. MODIS collection 6 MAIAC algorithm. *Atmos. Meas. Tech.* **2018**, *11*, 5741–5765. [CrossRef]
43. Hsu, N.C.; Herman, J.R.; Tsay, S.C. Radiative impacts from biomass burning in the presence of clouds during boreal spring in Southeast Asia. *Geophys. Res. Lett.* **2003**, *30*, 5. [CrossRef]
44. Sayer, A.M.; Munchak, L.A.; Hsu, N.C.; Levy, R.C.; Bettenhausen, C.; Jeong, M.J. MODIS Collection 6 aerosol products: Comparison between Aqua's Deep Blue, Dark Target, and "merged" datasets, and usage recommendations. *J. Geophys. Res. Atmos.* **2014**, *119*, 13965–13989. [CrossRef]
45. Jackson, J.M.; Liu, H.; Laszlo, I.; Kondragunta, S.; Remer, L.A.; Huang, J.; Huang, H.C. Suomi-NPP VIIRS aerosol algorithms and data products. *J. Geophys. Res. Atmos.* **2013**, *118*, 12673. [CrossRef]
46. Lee, K.H.; Kim, Y.J. Satellite remote sensing of Asian aerosols: A case study of clean, polluted, and Asian dust storm days. *Atmos. Meas. Tech.* **2010**, *3*, 1771–1784. [CrossRef]
47. Adesina, J.A.; Piketh, S.J.; Formenti, P.; Maggs-Kölling, G.; Holben, B.N.; Sorokin, M.G. Aerosol optical properties and direct radiative effect over Gobabeb, Namibia. *Clean Air J.* **2019**, *29*, 1–11. [CrossRef]
48. Tu, Q.; Hao, Z.; Yan, Y.; Tao, B.; Chung, C.; Kim, S. Aerosol optical properties around the East China Seas based on AERONET measurements. *Atmosphere* **2021**, *12*, 642. [CrossRef]
49. Ricchiazzi, P.; Yang, S.; Gautier, C.; Sowle, D. SBDART: A research and teaching software tool for plane-parallel radiative transfer in the Earth's atmosphere. *Bull. Am. Meteor. Soc.* **1998**, *79*, 2101–2114. [CrossRef]
50. Mayer, B.; Kylling, A. The libRadtran software package for radiative transfer calculations—Description and examples of use. *Atmos. Chem. Phys.* **2005**, *5*, 1855–1877. [CrossRef]
51. Kim, M.; Kim, J.; Wong, M.S.; Yoon, J.; Lee, J.; Wu, D.; Chan, P.W.; Nichol, J.E.; Chung, C.Y.; Ou, M.L. Improvement of aerosol optical depth retrieval over Hong Kong from a geostationary meteorological satellite using critical reflectance with background optical depth correction. *Remote Sens. Environ.* **2014**, *142*, 176–187. [CrossRef]
52. Koepke, P. Effective reflectance of oceanic whitecaps. *Appl. Opt.* **1984**, *23*, 1816–1824. [CrossRef] [PubMed]
53. Monahan, E.C.; Muircheartaigh, I. Optimal power-law description of oceanic whitecap coverage dependence on wind speed. *J. Phys. Oceanogr.* **1980**, *10*, 2094–2099. [CrossRef]
54. Cox, C.; Munk, W. Measurement of the roughness of the sea surface from photographs of the sun's glitter. *J. Opt. Soc. Am.* **1954**, *44*, 838–850. [CrossRef]
55. Morel, A. In-water and remote measurements of ocean color. *Bound.-Lay. Meteorol.* **1980**, *18*, 177–201. [CrossRef]
56. Costa, M.J.; Cervino, M.; Cattani, E.; Torricella, F.; Levizzani, V.; Silva, A.M. Aerosol optical thickness and classification: Use of METEOSAT, GOME, and modeled data. In *Satellite Remote Sensing of Clouds and the Atmosphere IV*; SPIE: Bellingham, WA, USA, 1999; Volume 3867, pp. 268–279. [CrossRef]

57. Kaufman, Y.J.; Tanré, D. *Algorithm for Remote Sensing of Tropospheric Aerosol from MODIS. NASA MODIS Algorithm Theoretical Basis Document*; Goddard Space Flight Center: Washington, DC, USA, 1998; Volume 85, pp. 3–68.
58. Torricella, F.; Cattani, E.; Cervino, M.; Guzzi, R.; Levoni, C. Retrieval of aerosol properties over the ocean using global ozone monitoring experiment measurements: Method and applications to test cases. *J. Geophys. Res. Atmos.* **1999**, *104*, 12085–12098. [CrossRef]
59. McRoberts, R.E. Diagnostic tools for nearest neighbors techniques when used with satellite imagery. *Remote Sens. Environ.* **2009**, *113*, 489–499. [CrossRef]
60. Kang, N.; Deng, F.; Khan, R.; Kumar, K.R.; Hu, K.; Yu, X.; Wang, X.; Devi, N.L. Temporal variations of PM concentrations, and its association with AOD and meteorology observed in Nanjing during the autumn and winter seasons of 2014–2017. *J. Atmos. Sol.-Terr. Phys.* **2020**, *203*, 105273. [CrossRef]
61. Draxler, R.R.; Rolph, G.D. *HYSPLIT (HYbrid Single-Particle Lagrangian Integrated Trajectory) Model Access via NOAA ARL READY Website*; NOAA Air Resources Laboratory: Silver Spring, MD, USA, 2010; Volume 25.
62. Wang, Y.Q.; Zhang, X.Y.; Draxler, R.R. TrajStat: GIS-based software that uses various trajectory statistical analysis methods to identify potential sources from long-term air pollution measurement data. *Environ. Model. Softw.* **2009**, *24*, 938–939. [CrossRef]
63. You, W.; Zang, Z.; Zhang, L.; Li, Z.; Chen, D.; Zhang, G. Estimating ground-level PM10 concentration in northwestern China using geographically weighted regression based on satellite AOD combined with CALIPSO and MODIS fire count. *Remote Sens. Environ.* **2015**, *168*, 276–285. [CrossRef]
64. Ranjan, R.R.; Joshi, H.P.; Iyer, K.N. Spectral variation of total column aerosol optical depth over Rajkot: A tropical semi-arid Indian station. *Aerosol Air Qual. Res.* **2007**, *7*, 33–45. [CrossRef]
65. Huang, Z.; Cui, F.; Kang, H.; Chen, J.; Xia, C. Characterization and catalytic properties of the CuO/SiO_2 catalysts prepared by precipitation-gel method in the hydrogenolysis of glycerol to 1,2-propanediol: Effect of residual sodium. *Appl. Catal. A Gen.* **2009**, *366*, 288–298. [CrossRef]
66. Filonchyk, M.; Yan, H. The characteristics of air pollutants during different seasons in the urban area of Lanzhou, Northwest China. *Environ. Earth Sci.* **2018**, *77*, 1–17. [CrossRef]
67. Shen, L.; Wang, H.; Kong, X.; Zhang, C.; Shi, S.; Zhu, B. Characterization of black carbon aerosol in the Yangtze River Delta, China: Seasonal variation and source apportionment. *Atmos. Pollut. Res.* **2021**, *12*, 195–209. [CrossRef]
68. Wang, Y.; Wang, X.; Kondo, Y.; Kajino, M.; Munger, J.W.; Hao, J. Black carbon and its correlation with trace gases at a rural site in Beijing: Top-down constraints from ambient measurements on bottom-up emissions. *J. Geophys. Res. Atmos.* **2011**, *116*, D24. [CrossRef]
69. Zhang, Q.; Ma, Q.; Zhao, B.; Liu, X.; Wang, Y.; Jia, B.; Zhang, X. Winter haze over North China Plain from 2009 to 2016: Influence of emission and meteorology. *Environ. Pollut.* **2018**, *242*, 1308–1318. [CrossRef]
70. Rajput, P.; Sarin, M.; Sharma, D.; Singh, D. Characteristics and emission budget of carbonaceous species from post-harvest agricultural-waste burning in source region of the Indo-Gangetic Plain. In *Air Quality*; Apple Academic Press: Waretown, NJ, USA, 2016; pp. 271–292.
71. Che, H.; Zhao, H.; Wu, Y.; Xia, X.; Zhu, J.; Dubovik, O.; Estelles, V.; Ma, Y.; Wang, Y.; Wang, H.; et al. Application of aerosol optical properties to estimate aerosol type from ground-based remote sensing observation at urban area of northeastern China. *J. Atmos. Sol.-Terr. Phys.* **2015**, *132*, 37–47. [CrossRef]
72. Cui, S.; Xian, J.; Shen, F.; Zhang, L.; Deng, B.; Zhang, Y.; Ge, X. One-year real-time measurement of black carbon in the rural area of Qingdao, Northeastern China: Seasonal variations, meteorological effects, and the COVID-19 case analysis. *Atmosphere* **2021**, *12*, 394. [CrossRef]
73. Zhu, Y.; Sabaliauskas, K.; Liu, X.; Meng, H.; Gao, H.; Jeong, C.H.; Evans, G.J.; Yao, X. Comparative analysis of new particle formation events in less and severely polluted urban atmosphere. *Atmos. Environ.* **2014**, *98*, 655–664. [CrossRef]
74. Dubovik, O.; Holben, B.; Eck, T.F.; Smirnov, A.; Kaufman, Y.J.; King, M.D.; Tanré, D.; Slutsker, I. Variability of absorption and optical properties of key aerosol types observed in worldwide locations. *J. Atmos. Sci.* **2022**, *59*, 590–608. [CrossRef]
75. Yoon, S.C.; Kim, J. Influences of relative humidity on aerosol optical properties and aerosol radiative forcing during ACE-Asia. *Atmos. Environ.* **2006**, *40*, 4328–4338. [CrossRef]
76. Aas, E.C.R. Importance of Meteorology on Dispersion of Air Pollution in the Surface Layer. The Use of Modeled and Observed Meteorology in Dispersion Models. Master's Thesis, University of Oslo, Oslo, Norway, 2018.
77. Kant, S.; Panda, J.; Gautam, R. A seasonal analysis of aerosol-cloud-radiation interaction over Indian region during 2000–2017. *Atmos. Environ.* **2019**, *201*, 212–222. [CrossRef]
78. Duan, J.; Mao, J.T. Study on the distribution and variation trends of atmospheric aerosol optical depth over the Yangtze River Delta. *Acta Sci. Circumstantiae* **2007**, *27*, 537–543. [CrossRef]
79. He, Q.; Li, C.; Geng, F.; Yang, H.; Li, P.; Li, T.; Liu, D.; Pei, Z. Aerosol optical properties retrieved from Sun photometer measurements over Shanghai, China. *J. Geophys. Res. Atmos.* **2012**, *117*, D16. [CrossRef]

80. Zhuang, B.; Wang, T.; Liu, J.; Li, S.; Xie, M.; Han, Y.; Chen, P.; Hu, Q.; Yang, X.Q.; Fu, C.; et al. The surface aerosol optical properties in the urban area of Nanjing, west Yangtze River Delta, China. *Atmos. Chem. Phys.* **2017**, *17*, 1143–1160. [CrossRef]
81. Abuelgasim, A.; Bilal, M.; Alfaki, I.A. Spatiotemporal variations and long-term trends analysis of aerosol optical depth over the United Arab Emirates. *Remote Sens. Appl. Soc. Environ.* **2021**, *23*, 100532. [CrossRef]
82. Begum, B.A.; Hossain, A.; Nahar, N.; Markwitz, A.; Hopke, P.K. Organic and black carbon in $PM_{2.5}$ at an urban site at Dhaka, Bangladesh. *Aerosol Air Qual. Res.* **2012**, *12*, 1062–1072. [CrossRef]
83. Cha, Y.; Lee, S.; Lee, J. Measurement of black carbon concentration and comparison with PM_{10} and $PM_{2.5}$ concentrations monitored in Chungcheong province, Korea. *Aerosol Air Qual. Res.* **2019**, *19*, 541–547. [CrossRef]
84. Heo, J.; Antkiewicz, D.S.; Shafer, M.M.; Perkins, D.A.; Sioutas, C.; Schauer, J.J. Assessing the role of chemical components in cellular responses to atmospheric particle matter (PM) through chemical fractionation of PM extracts. *Anal. Bioanal. Chem.* **2015**, *407*, 5953–5963. [CrossRef]
85. Holben, B.N.; Tanré, D.; Smirnov, A.; Eck, T.F.; Slutsker, I.; Abuhassan, N.; Newcomb, W.W.; Schafer, J.S.; Chatenet, B.; Lavenu, F.J.; et al. An emerging ground-based aerosol climatology: Aerosol optical depth from AERONET. *J. Geophys. Res. Atmos.* **2001**, *106*, 12067–12097. [CrossRef]
86. Rosen, H.; Hansen, A.D.A.; Gundel, L.; Novakov, T. Identification of the optically absorbing component in urban aerosols. *Appl. Opt.* **1978**, *17*, 3859–3861. [CrossRef] [PubMed]
87. Sinha, P.R.; Dumka, U.C.; Manchanda, R.K.; Kaskaoutis, D.G.; Sreenivasan, S.; Krishna Moorthy, K.; Suresh Babu, S. Contrasting aerosol characteristics and radiative forcing over Hyderabad, India due to seasonal mesoscale and synoptic-scale processes. *Quart. J. R. Meteorol. Soc.* **2013**, *139*, 434–450. [CrossRef]
88. Tiwari, S.; Kaskaoutis, D.; Soni, V.K.; Dev Attri, S.; Singh, A.K. Aerosol columnar characteristics and their heterogeneous nature over Varanasi, in the central Ganges valley. *Environ. Sci. Pollut. Res.* **2018**, *25*, 24726–24745. [CrossRef] [PubMed]